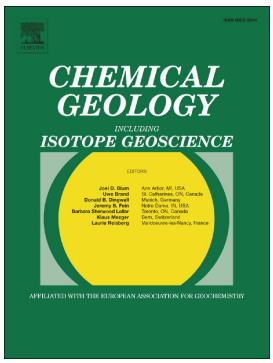
Journal Pre-proof



U-Pb systematics of uranium-rich apatite from Adirondacks: Inferences about regional geological and geochemical evolution, and evaluation of apatite reference materials for in situ dating

Evgenii Krestianinov, Yuri Amelin, Leonid A. Neymark, John N. Aleinikoff

PII: S0009-2541(21)00360-0

DOI: https://doi.org/10.1016/j.chemgeo.2021.120417

Reference: CHEMGE 120417

To appear in: *Chemical Geology*

Received date: 11 November 2020

Revised date: 2 July 2021

Accepted date: 4 July 2021

Please cite this article as: E. Krestianinov, Y. Amelin, L.A. Neymark, et al., U-Pb systematics of uranium-rich apatite from Adirondacks: Inferences about regional geological and geochemical evolution, and evaluation of apatite reference materials for in situ dating, *Chemical Geology* (2018), https://doi.org/10.1016/j.chemgeo.2021.120417

This is a PDF file of an article that has undergone enhancements after acceptance, such as the addition of a cover page and metadata, and formatting for readability, but it is not yet the definitive version of record. This version will undergo additional copyediting, typesetting and review before it is published in its final form, but we are providing this version to give early visibility of the article. Please note that, during the production process, errors may be discovered which could affect the content, and all legal disclaimers that apply to the journal pertain.

© 2018 © 2021 Published by Elsevier B.V.

Journal Pre-proof

U-Pb systematics of uranium-rich apatite from Adirondacks: inferences about regional geological and geochemical evolution, and evaluation of apatite reference materials for *in situ* dating.

Evgenii Krestianinov[1*], Yuri Amelin[1], Leonid A. Neymark[2], John N. Aleinikoff[2]

[1]*Research School of Earth Sciences, Australian National University, Canberra, 2601, Australia*

[2]*U.S. Geological Survey, Denver, CO, USA*

* Corresponding author

E-mail address: *evgenii.krestianinov@anu.edu.au* (E. Krestianinov)

Journal Pre-proof

1. Introduction

Apatite is a common accessory mineral in igneous, metamorphic, and sedimentary rocks. Numerous studies have shown that trace element concentrations, rare earth element (REE) patterns, and elemental and isotopic compositions of halogens in apatite provide information about crystallization environment and source rocks (e.g., BELOUSOVA et al., 2002; PAN et al., 2016; ANDERSSON et al., 2019; ANSBERQUE et al., 2019; O'SULLIVAN et al., 2020). Apatite is a valuable mineral for tracking crustal evolution (BRUAND et al., 2020; O'SULLIVAN AND CHEW, 2020), sedimentary provenance studies (CHEW et al., 2011), and for mineral exploration (MAO et al., 2016). It has also been widely used in geochronology and thermochronology studies because it usually preferentially incorporates U, Th, Sm and Lu relative to Pb, He and Hf during crystal growth, and hence has high parent/daughter isotope ratios for several decay schemes with different closure temperatures, including U-Th-Sm/He (40-80°C), fission track (60-110°C), U-Pb (350-550°C), Lu-Hf (675-750°C), and U-series disequilibrium dating (CHEW AND SPIKINGS, 2015). These closure temperatures are estimated from experimental studies for U-Th-Sm/He (FARLEY, 2000; VAN SOEST et al., 2011) and fission track (e.g., LASLETT et al., 1987) dating; from empirical studies for Lu-Hf system (e.g., BARFOD et al., 2005), or from both for U-Th-Pb system (CHERNIAK et al., 1991; CHAMBERLAIN AND BOWRING, 2001) and depend on crystal size and shape, cooling rate, and probably on the composition of apatite, particularly F, Cl and OH contents (e.g. GREEN et al., 1986; BARBARAND et al., 2003).

Apatite is often dated by *in situ* methods, including laser ablation-inductively coupled plasma mass spectrometry (LA-ICPMS) and secondary ion mass spectrometry (SIMS), due to the rapid throughput of these methods as compared to isotope dilution-thermal ionization mass spectrometry (ID-TIMS) measurements. However, because of larger sample size, the absence of matrix effects, and independence from external calibration material, ID-TIMS results are far more precise than LA-ICPMS or SIMS data.

Accurate age determinations by LA-ICPMS and SIMS require matrix-matched reference materials (RM) with a similar composition, similar range of U and Th concentrations, ablation response, and precisely and accurately known ages that are preferably in a similar range to the ages of unknowns (e.g., BLACK et al., 2004). Use of an apatite RM that has similar U and Th content to the unknowns yields the highest precision because the analyst can optimize laser beam spot size in LA-ICPMS or primary ion beam aperture in SIMS for obtaining optimal and comparable count rates for both standards and unknowns. The main

purpose of this study is to use high-precision U-Pb ID-TIMS geochronology of high-U (up to 300-500 ppm) apatite to determine its suitability as a reference material for *in situ* dating of apatite unknowns with high-U concentrations. Use of high-U apatite allows reduction of the primary beam size for better estimation of sample heterogeneity (though decreasing the beam size will increase downhole fractionation due to the smaller diameter to depth ratio, e.g. MANK AND MASON, 1999), improved counting statistics, reduced matrix effects, and decreased age uncertainty of a reference material, which is then propagated to the age uncertainty of unknowns. The usage of such RMs would be particularly beneficial for LA-ICPMS with quadrupole mass analysers (LA-Q-ICPMS) which have lower sensitivity than sector field LA-ICPMS (VANHAECKE, 2012), and therefore require a larger laser beam size for achieving sufficiently high ion counting rates and therefore better precision.

There are several apatite geochronological primary reference materials that are currently in use (Table 1). Three of them, McClure Mountain (MMap), Durango, and Madagascar (MAD) were used in this study; data for some other less frequently employed RMs were presented by CHEW et al. (2011). Unfortunately, only a few apatite RMs have been dated by U-Pb ID-TIMS. In addition, existing RMs do not cover a wide range of concentrations that can be observed in apatite samples and, therefore, more reference apatite samples are needed to fill the concentration gaps. Moreover, the precision and accuracy of the ages of analysed apatite RMs need further verification and improvement.

We have dated three apatite samples by ID-TIMS, sector field LA-ICPMS and SIMS methods: McClure Mountain apatite (MMap, SCHOENE AND BOWRING, 2006), and two apatites from iron oxide-apatite (IOA) deposits (Cheever mine (CM) and Old Bed mine (OBM), eastern Adirondacks, NY; LUPULESCU et al., 2017). The CM and OBM samples have high REE and U contents and, therefore, were investigated as potential primary reference materials for geochronology of apatite unknowns with similarly elevated REE and U concentrations (see section 5.4). Our age data for apatite from IOA deposits in the eastern Adirondacks also help to elucidate geological history of the region. Additional ID-TIMS analyses of the McClure Mountain apatite were conducted to refine previous results for this widely used reference material.

2. Geological setting and previous geochronology

2.1. Eastern Adirondacks, NY

The Cheever and Old Bed mines are located in the eastern Adirondack Mountains, NY, USA, which are part of the Mesoproterozoic Grenville Province (Fig. 1). Based on metamorphic grade and lithology, the Adirondack Mountains have been subdivided into the Highlands (AH, upper amphibolite- to granulite-grade rocks) and Northwest Lowlands (AL, amphibolite-grade rocks), which are separated by the northeast-trending Carthage-Colton shear zone (MCLELLAND et al., 2013). Adirondack Highlands metasedimentary rocks were intruded by magmatic rocks. CHIARENZELLI AND MCLELLAND (1991) subdivided them into five groups based on age and composition: tonalitic and trondhjemitic rocks, early calcalkaline plutonic rocks, anorthosite-mangerite-charnockite-granite (AMCG) suite, syn- to late-tectonic granite rocks, and late to post-tectonic fayalite granite. RIVERS (2015) interpreted AH as part of a medium pressure belt in the mid crust beneath the orogenic lid represented by the AL.

The IOA deposits of the eastern Adirondacks are located in the AH zone and mostly occur within the Lyon Mountain Granite Gneiss (LMG, previously thought to be ~1050 Ma, MCLELLAND et al., 2001; VALLEY et al., 2011, but now re-interpreted to have been emplaced at ~1150 Ma, ALEINIKOFF et al., 2021). The iron ores of the eastern Adirondacks consist of intrusive sheets or dikes composed of low-Ti magnetite associated with fluorapatite, augitic pyroxenes, and trace minerals including zircon, stillwellite, monazite, and allanite. Iron oxide-apatite deposits cross-cut all lithologies except late pegmatites, which cross-cut some ore bodies and are dated at about 1040 to 1020 Ma (LUPULESCU et al., 2011). Detailed geological descriptions of the deposits are given in VALLEY et al. (2011), MCLELLAND et al. (2013) CHIARENZELLI et al. (2018), REGAN et al. (2019) and references therein.

As summarized in VALLEY et al. (2011), models for the origin of Adirondack low-Ti iron ore deposits include immiscible magmatic Fe-rich fluids (POSTEL, 1952), breakdown of pre-existing mafic silicates (HAGNER AND COLLINS, 1967), eruption of Fe oxide lavas (WHITNEY AND OLMSTED, 1993), and interaction of surface-derived saline fluids with latest-stage plutonic emplacement (MCLELLAND et al., 2002). The LMG was proposed as the source of heat and fluid and served as the host rock for most of the eastern Adirondack low-Ti iron deposits. Based on an interpreted age of ~1050 Ma for LMG (MCLELLAND et al., 2001), VALLEY et al. (2011) concluded that the Fe mineralization continued to accumulate due to Na-rich fluid alteration over tens of millions of years after crystallization of the host rocks. However, this model requires revision because the LMG has now been shown to have crystallized at least 100 Ma prior to formation of the Fe deposits of the eastern Adirondacks

(ALEINIKOFF et al., 2021). TAYLOR et al. (2019) suggested that multiple episodes of hydrothermal alteration were responsible for formation of apatite in low-Ti magnetite deposits. Ore of these deposits is composed of magnetite, fluorapatite, hematite and clinopyroxene, with accessory monazite, allanite, edenite, titanite, ilmenite, hematite and scapolite (LUPULESCU et al., 2017).

Ages for zircon from low-Ti iron deposits are: (1) 1034 ± 3 Ma (LA-ICPMS data, CHIARENZELLI et al., 2018); (2) 1043 ± 12 (LA-ICPMS data, LUPULESCU et al., 2016); (3) 1059 ± 7, 1028 ± 5 and 1007 ± 4 Ma (SIMS data, Blacksmith mine, ALEINIKOFF AND WALSH, 2016); (4) 1030 ± 12, 1022 ± 10 and 996 ± 8 Ma (SIMS data, Schofield mine, ALEINIKOFF AND WALSH, 2016); (5) 1039 ± 4 Ma (Palmer mine), 1016 ± 7 Ma (Arnold Hill mine), 1001 ± 9 Ma (Skiff Mtn. mine), and 1001 ± 4 Ma (SIMS data, Old Bed mine, VALLEY et al., 2009). In addition, monazite that formed due to dissolution-reprecipitation of apatite yielded an age of 980 ± 5.8 Ma (REGAN et al., 2019). These data suggest a protracted history of formation of IOA deposits in the eastern Adirondacks.

The ^{207}Pb-corrected U-Pb age of apatite from IOA deposits at Mineville in Adirondacks was estimated by LA-ICPMS at 1009 ± 15 Ma (CHEW et al., 2011) using a Stacey-Kramers (1975; hereafter shown as S-K) common-Pb model for initial Pb correction. Apatite samples from the Cheever and Old Bed mines have not been previously dated by high-precision U-Pb ID-TIMS methods.

2.2. McClure Mountain complex

The McClure Mountain complex is located in the Wet Mountains region, Fremont County, south-central Colorado, USA, and consists of 1.70-1.36 Ga Proterozoic gneiss and granitic rocks that host several alkaline igneous complexes of early Cambrian age, including McClure Mountain, Gem Park, Democrat Creek, and Iron Mountain (OLSON et al., 1977; ARMBRUSTMACHER AND HEDGE, 1982; ARMBRUSTMACHER, 1984). The McClure Mountain complex is the largest of the igneous bodies and is bimodal in composition, composed of a mafic-ultramafic zone emplaced in the northeast and a younger larger alkaline massif (SHAWE AND PARKER, 1967). Dikes of carbonatitic, lamprophyric, and trachytic composition cross-cut these Precambrian and Cambrian rocks (HEINRICH AND DAHLEM, 1969).

Chronological data for rocks of the McClure Mountain complex were obtained using various isotopic systems. All geochronological data published before 2010 can be found in Geochronology database for central Colorado (KLEIN et al., 2010). OLSON et al. (1977)

reported the following results: K-Ar hornblende and biotite ages of 520 and 508 Ma, respectively, and a Rb-Sr age of 521 ± 10 Ma. BICKFORD et al. (1989) reported multi-grain TIMS U-Pb zircon age of 536 ± 4 Ma. McClure Mountain syenite, the source of $^{40}Ar/^{39}Ar$ hornblende reference material MMhb, yielded Ar-Ar ages of 520.4 ± 1.7 Ma (SAMSON AND ALEXANDER, 1987), 523.1 ± 2.6 Ma (RENNE et al., 1998), 523.2 ± 0.9 Ma (SPELL AND MCDOUGALL, 2003). PIVARUNAS AND MEERT (2019) reported LA-ICPMS U-Pb zircon ages of 526 ± 8 Ma and 483 ± 2 Ma from lamprophyric and trachytic dikes, respectively. High-precision ID-TIMS U-Pb dating results for the McClure Mountain syenite complex have been reported by SCHOENE AND BOWRING (2006). Mineral ages are: (1) 523.98 ± 0.12 Ma for zircon, (2) 523.26 ± 0.65 Ma for titanite - assuming an initial Pb composition of $^{206}Pb/^{204}Pb$ = 17.79 ± 0.34, $^{207}Pb/^{204}Pb$ = 15.56 ± 0.10, and (3) 523.51 ± 1.47 Ma for apatite assuming an initial Pb composition of $^{206}Pb/^{204}Pb$ = 17.54 ± 0.27, $^{207}Pb/^{204}Pb$ = 15.47 ± 0.04. The agreement of all three ages indicates fast cooling of this syenite pluton. Apatite from the McClure Mountain syenite (MMap) has been widely used as a matrix-matched reference material for *in situ* U-Pb dating (e.g. THOMSON et al., 2012; CHEW et al., 2016; KIRKLAND et al., 2018; O'SULLIVAN AND CHEW, 2020). Because the accepted age was based only on six data points after eliminating one outlier, we decided to collect more ID-TIMS U-Pb data for the MMap to verify, and possibly refine, the currently accepted age.

3. Methods

3.1. Scanning electron microscopy (SEM) and electron probe microanalysis (EPMA)

Handpicked apatite grains for backscattered electrons (BSE) imaging and EPMA were mounted in epoxy, ground with sandpaper to about half-thickness, and polished with 3- and 1-µm diamond pastes. Before EPMA, all grains were BSE-imaged using SEM to reveal possible complex textures, using the JEOL JSM 6610A microscope at the Research School of Earth Sciences (RSES), Australian National University.

After imaging, apatite grains were analysed for major and minor elements at the Centre for Advanced Microscopy (CAM), ANU, using a JEOL 8530F Plus microprobe analyser. Major elements were analysed with an accelerating voltage of 15kV, a beam current of 10 nA, and a beam size of 15 µm. Minor and trace elements were measured using the same parameters except a beam current of 100 nA. After quantitative analysis, selected apatite grains from CM and OBM were analyzed for elemental mapping to reveal the distribution of Th, Si, Y and Sr. After EPMA, the mount was cleaned and re-polished for analysis of trace elements by LA-ICPMS.

3.2. LA-ICPMS trace elements analysis

Trace elements of apatite samples CM, OBM, and MMap were analysed by LA-ICPMS at RSES using LPF Pro 202 laser ablation system (193 nm) with a HelEx cell coupled to an Agilent 7700 quadrupole ICPMS. The laser was set with a spot size of 22 µm; baselines were measured for 20 s and peaks were measured for 30 s of ablation. A suite of 55 elements was analysed with the main focus on U, Th, and Pb. The NIST612 and NIST614 glasses were used as primary and secondary reference materials, respectively. Calcium concentrations from EPMA analyses were used as internal standard. Data processing was done with the software package Iolite™ 4 (PATON et al., 2011).

3.3. ID-TIMS

For this study, MMap, CM and OBM apatite samples were analysed by the single-grain ID-TIMS method at the SPIDE^{2}R lab, RSES. Apatite grains (fourteen grains from CM, sixteen grains from OBM, fourteen single grains plus six fragments of three grains each from MMap with approximate weights of 6-127 µg) without visible inclusions or cracks were handpicked under a binocular microscope, ultrasonically cleaned with ethanol (30 min), rinsed with distilled acetone three times, and weighed before being loaded into Teflon vials. The samples were spiked with a ^{202}Pb-^{205}Pb-^{233}U-^{236}U tracer and dissolved in 200 µl of 6M HCl on a hot plate for 12-14 h at 110°C, then redissolved in 200 µl 0.5M HCl and 10 µl 9M HBr. Pb was separated using HBr column chemistry with Eichrom AG1x8 resin (AMELIN et al., 2019). U was separated using HNO_3 column chemistry with Eichrom UTeva resin. All samples were evaporated with 50 µl of 0.02N H_3PO_4 and loaded onto Re filaments with Aldrich silica gel (HUYSKENS et al., 2012).

Pb and U isotopic compositions were measured on the TritonPlus™ thermal ionization mass-spectrometer. Pb was measured in static Faraday mode; samples with low ^{204}Pb were measured by secondary electron multiplier detector. Uranium was measured as UO_2^+ in secondary electron multiplier mode. The quality of analyses was monitored by analysis of Pb isotopic standard SRM-981, and EARTHTIME-100 and EARTHTIME-500 U-Pb synthetic reference solutions. The summary of our results for the EARTHTIME standards was reported by CARR et al. (2020).

The total procedural blanks of all analytical sessions were 0.20-0.42 pg Pb and 0.01-0.07 pg U. These values were used in the data reduction using a modified version of the AnySpike software (SCHMITZ AND SCHOENE, 2007). Reduced ID-TIMS data were plotted using Isoplot

3.75 (LUDWIG, 2012) on four types of isochron diagrams: $^{206}Pb/^{204}Pb$ vs. $^{238}U/^{204}Pb$, $^{207}Pb/^{204}Pb$ vs. $^{235}U/^{204}Pb$, total Pb/U (LUDWIG, 1998), and Tera-Wasserburg (TERA AND WASSERBURG, 1972), and in Concordia diagram (WETHERILL, 1956).

3.4. *In situ* U-Pb analyses

Handpicked apatite grains were analysed by laser ablation sector-field LA-ICPMS, and apatite and zircon grains were analysed by SIMS (using either the U.S. Geological Survey (USGS)/Stanford sensitive high-resolution ion microprobe-reverse geometry SHRIMP-RG or the Geological Survey of Canada, Ottawa SHRIMP II). The grains were placed onto double-sided tape under a binocular microscope, mounted in epoxy, ground to about half-thickness using 1,500- or 2,500-grit sandpaper, and polished sequentially using 6- and 1-µm diamond suspensions. The mount was then rinsed with DI water and alcohol. Before *in situ* analysis, all samples were imaged in transmitted and/or reflected light on a petrographic microscope and examined for compositional zoning and the presence of inclusions by BSE and cathodoluminescence (CL) imagery using the JEOL 5800LV SEM at the USGS Microbeam Laboratory in Denver.

3.4.1. LA-ICPMS

LA-ICPMS analyses of apatite were conducted using a Nu Instruments sector-field AttoM™ mass spectrometer at the USGS Plasma Laboratory in Denver. Grains were ablated with a Photon Machines Excite™ 193 nm ArF excimer laser in spot mode (150 total bursts per spot analysis) with a repetition rate of 5 Hz, laser energy of 3-5 mJ, and an energy density of 4-5 J/cm^2. The rate of He gas flow to the HelEx cell of the laser was 0.25-0.40 L/min and make-up Ar gas (0.21-0.29 L/min) was added to the sample stream prior to introduction into the plasma. As suggested by HU et al. (2008), nitrogen with a flow rate of 5.5 mL/min was added to the sample stream, which allowed for a significant reduction in ThO+/Th+ (< 0.5%) and improved the ionization efficiency of Th. The laser spot sizes were 50-85 and 20-25 µm in diameter for low-U and high-U apatite, respectively. With the magnet parked at a constant mass, the flat tops of the isotope peaks were measured by secondary electron multiplier at the following masses by rapid deflection of the ion beam: ^{202}Hg, ^{204}(Hg + Pb), ^{206}Pb, ^{207}Pb, ^{208}Pb, ^{232}Th, ^{235}U, and ^{238}U; on-peak backgrounds were measured for 30 s prior to each 30- to 60-s analysis. For high-Th apatite samples, the ^{232}Th peak was excluded from the analytical sequence to avoid ion beam attenuation. Raw data were reduced off-line using the U-Pb geochronology Data Reduction Scheme (DRS) U_Pb_Geochronology3 of the Iolite™ 2.5

program (PATON et al., 2011) to subtract on-peak background signals, correct for mass-discrimination in measured Pb-isotope ratios, U-Pb downhole fractionation, and normalization of instrumental mass bias using National Institute of Standards (NIST) SRM 610 and NIST SRM-612 glasses as primary matrix-unmatched reference materials (for high-U and low-U apatite, respectively). Each analytical session consisted of alternating five spot analyses of the NIST glass followed by five spot analyses of a primary apatite matrix-matched reference, five spot analyses of unknowns, and five spot analyses of a secondary apatite reference. Typically, ≥ 30 spot analyses for each material were conducted in an analytical session. Approximate U and Th concentrations in the matrix-matched apatite references and unknowns were calculated by Iolite™ using the NIST glasses as the primary standard reference materials for which U and Th concentrations were certified by NIST. Because of the matrix difference between the NIST glasses and apatite we assumed the U and Th concentration data to be not better than ± 20% accurate based on results by JOCHUM AND STOLL (2008). The matrix-matched apatite references MMAp and MAD, ages of which had previously been determined by ID-TIMS, were analysed with unknowns with U contents ≤ 300 ppm. For analysis of high-U apatite unknowns (> 300 ppm), OBM apatite was used as a primary matrix-matched reference material by accepting its ID-TIMS age of 924 ± 13 Ma (this study, section 4.1.2.).

We compared our two-stage data reduction approach that uses NIST glass to correct for Pb-isotope fractionation and a matrix-matched reference apatite to correct for elemental fractionation as it was described in detail in NEYMARK et al. (2016) with the data reduction using UcomPbine DRS (CHEW et al., 2014) in Iolite 4. The data for low-U OBM in analytical session T8400 (Table EA5) where MMAp was used as a matrix-matched reference apatite were reduced using both methods. The UcomPbine DRS that uses fixed Pb_c $^{207}Pb/^{206}Pb$ value for MMAp of 0.88198 (no uncertainty assigned) in its suggested MMAp standard file yielded OBM age of 853 ± 27 Ma. This value is younger (although marginally within error) with the value of 897 ± 27 Ma reported in our paper. We used their recommended Pb_c composition to re-reduce the data using an anchored T-W isochron for the MMAp and obtained the age value of 848 ± 36 Ma, which is within error of the UcomPbine value. The date from our calculation has larger uncertainty because the uncertainty of the measured initial Pb value was included in the error propagation. Both approaches yielded identical dates, 897 ± 27 Ma for our method (Fig. 11A), and 897 ± 26 Ma for UcomPbine DRS if the measured in this analytical session Pb_c value of $^{207}Pb/^{206}Pb$ = 0.806 ± 0.054 is used instead of the value recommended in

Iolite 4. This example shows that the usage of the measured Pb_c yields more accurate age estimate which is within error of the ID-TIMS age of 924 ± 14 Ma for the OBM apatite.

Reduction of apatite LA-ICPMS data is often complicated by variable incorporation of non-radiogenic Pb in the unknowns and the reference apatites. It was shown (SOUDERS AND SYLVESTER, 2010; PIETRUSZKA AND NEYMARK, 2017) that despite significant differences in the ablation behaviour of silicate glass and natural minerals, precise and accurate lead isotope ratio data can be obtained by LA-ICPMS using commonly available synthetic silicate glasses as calibration reference materials. Thus, we used Pb-isotope ratios calculated by Iolite™ for further data reduction and age calculations. Then, biased isotopic dates were calculated in Isoplot for the MMap, MAD, and OBM matrix-matched references by constructing unconstrained or anchored Tera-Wasserburg (T-W) isochrons (depending on the observed spread of the data points along the isochron). The Iolite™ output for $^{207}Pb/^{206}Pb$ and $^{238}U/^{206}Pb$ values was used as input data for Isoplot age calculations. A 500-Ma S-K model $^{207}Pb/^{206}Pb$ value of 0.87 ± 0.10 was used as a fixed Y axis intercept for MAD1 and MAD2 and $^{207}Pb/^{206}Pb$ value of 0.186 ± 0.018 determined by ID-TIMS (this study, see 4.1.2 chapter) was used for the OBM reference material. These dates differ from accepted ages for these materials because of the matrix-unmatched NIST glass standards were used in Iolite™ as primary references to calculate $^{238}U/^{206}Pb$ ratios.

The difference between the T-W isochron age and the "true" age of the matrix-matched apatite references is used to determine a correction factor ($F = {}^{238}U/^{206}Pb_{true}/^{238}U/^{206}Pb_{Iolite}$) for the U/Pb ratio for each analytical session. Lastly, the correction factor (F) is applied to calculate bias-corrected $^{238}U/^{206}Pb$ ratios for unknowns: $(^{238}U/^{206}Pb)_{corrected} = F \times (^{238}U/^{206}Pb)_{measured}$, where subscript "measured" corresponds to the NIST-normalized Iolite™ output values. These bias-corrected $^{238}U/^{206}Pb$ ratios and Iolite™ $^{207}Pb/^{206}Pb$ are used in Isoplot as input parameters for the T-W age calculations for apatite unknowns.

The bias-corrected $^{238}U/^{206}Pb$ ratios for individual spot analyses of the primary matrix-matched references were also calculated using these F values. Then, the bias-corrected $^{238}U/^{206}Pb$ ratios were used to construct T-W isochrons for these reference apatites, similarly to unknowns. This approach (here called "self-normalisation") does not allow an estimate of the accuracy of the LA-ICPMS analyses but helps to evaluate possible age heterogeneity of the reference material if these T-W isochrons show excess scatter (elevated MSWD values).

This self-normalisation approach also allows for comparison of different matrix-matched references based on uncertainties of the calculated ages.

3.4.2. SHRIMP

Zircon separated from sample OBM was run on the SHRIMP II at the Geological Survey of Canada (Ottawa, ON). Zircon reference material R33 (BLACK et al., 2004) was used to calibrate $^{206}Pb/^{238}U$ ages and Z1242 was used to correct for isotopic fractionation of $^{207}Pb/^{206}Pb$ ratios (DAVIS et al., 2018). OBM apatite was analysed using the USGS/Stanford SHRIMP-RG, following methods described by WILLIAMS (1998). For all analyses of zircon and apatite, the primary oxygen ion beam was focussed to about 20-25 µm in diameter. The magnet was cycled through the appropriate mass stations five times. Measured $^{206}Pb/^{238}U$ ratios for the OBM apatite were normalized to values for MAD1. No energy filtering was used during apatite analysis.

Both SHRIMP II and SHRIMP-RG data were reduced using the Squid 2 program (LUDWIG, 2009) and plotted using Isoplot 4.15 (LUDWIG, 2012). The initial Pb correction was applied using the S-K model values for 1 Ga Pb. All uncertainties on dates reported in this paper are ± 2SD unless noted otherwise.

4. Results

4.1. Apatite and zircon samples description and imaging

For this study, we analysed several apatite reference materials (MMap, MAD, and Durango) with published ages (Schoene and Bowring, 2006; Thomson et al., 2012; McDowell et al., 2005) as well as two higher-U apatite samples from the eastern Adirondack (CM and OBM) that have not been dated previously. We also analysed zircon separated from the OBM ore sample.

LUPULESCU et al. (2017) reported chemical compositions and described the main types of textures for apatite from the eastern Adirondack. Fluorapatite from these mines is characterized by high total REE (4.7 wt% in OBM and 6.5-15.7 wt% in CM), relatively elevated concentrations of U (270 ppm and 333-1057 ppm in OBM and CM, respectively), and Th (1224 ppm and 122-4290 ppm in OMB and CM, respectively) (Lupulescu et al., 2017). REE concentration correlates with SiO_2 content and some REE-rich apatite grains contain SiO_2 up to 5.7 wt.% with corresponding decrease of CaO and P_2O_5 concentrations. Cheever mine apatite has the highest concentrations of Mn (329-997 ppm), Sr (174-608 ppm)

and Pb (up to 270-290 ppm) as compared with other Adirondack IOA apatite samples (LUPULESCU et al., 2017). Because of the high-U contents, these samples may contain relatively high proportions of radiogenic lead, and therefore are good candidates for precise U-Pb geochronology, even for small sample sizes.

LUPULESCU et al. (2017) found four types of apatite textures: (1) low backscatter electron (BSE) intensity areas within brighter apatite grains or along margins. Such areas often associated with monazite inclusions and caused by metasomatic reworking of primary apatite (HARLOV, 2015); (2) low BSE intensity areas without monazite inclusions; (3) mantled apatite, where monazite, allanite and titanite form nearly continuous rims on apatite grains; (4) oscillatory zoned apatite, where some grains contain oscillatory zoned apatite clusters in a matrix of unzoned apatite.

Representative BSE images of the MMap, CM, and OBM apatite samples are presented in Fig. 2. Euhedral to subhedral crystals of MMap range in size from ~ 100 to 150 µm in length. BSE imaging reveals faint oscillatory zoning (Fig. 2A and B) in some grains, whereas others are relatively unzoned. Anhedral CM apatite grains of 150-350 µm in length contains BSE-dark domains mantled by BSE-light apatite (Fig. 2C), as described by LUPULESCU et al. (2017). Most of the grains show unzoned areas (Fig. 2D) or different shades of grey, with lighter tones reflecting greater average atomic number (Z value) and higher concentrations of REE, U, and Th. A likely cause of this patchy zoning is dissolution-reprecipitation processes which were described for Kiruna-type IOA deposit Kiirunavaara in northern Sweden (HARLOV et al., 2002) and also observed in experiments (e.g., HARLOV et al., 2005). Micron-sized monazite inclusions are observed along fractures (Fig. 2D) and in one grain we detected a zircon inclusion of 20*25 µm in size (see Table EA 1). The OBM apatite was separated from an ore sample mainly composed of magnetite (72 vol%), apatite (12 vol%) and quartz (4 vol%) based on the electron-microprobe mineral mapping. In addition to BSE imaging of individual grains, we investigated a thin section of OBM ore that shows abundant monazite inclusions in apatite associated with magnetite and quartz (Fig. 3A). This apatite is similar to apatite in sample CM, has unzoned areas (Fig. 2E), and contains magnetite inclusions (Fig. 2F), indicating that the apatite formed during or after formation of iron oxide. BSE imaging of OBM ore reveals that all apatite grains have been variably altered. Some apatite grains are relatively pristine (e.g., Fig. 3B), others contain altered and unaltered zones (Fig. 3D) or show abundant monazite in fractures (Fig. 3A and C).

The Old Bed ore contains dark brown, large (up to 10 mm), highly metamict zircon crystals. VALLEY et al. (2009) reported a range of $^{207}Pb/^{206}Pb$ SIMS U-Pb dates for these zircons and interpreted a weighted average of the four oldest samples of 1020 ± 11 Ma as the time of crystallisation. These authors interpreted younger dates as the result of Pb loss due to metamictisation and obtained a weighted average age of 1000.7 ± 4.2 Ma after excluding several youngest $^{207}Pb/^{206}Pb$ dates. Alternatively, it is possible that the older and younger ages reflect at least two episodes of formation. Because VALLEY et al. (2009) did not report U-Pb ages for OBM zircon and, therefore, a degree of the age discordance cannot be evaluated, we performed U-Pb SHRIMP analyses of OBM zircon separated from the same ore sample as the apatite.

4.2. Chemical composition of apatite

Major, minor, and trace element compositions of apatite, as well as REE patterns are presented in Tables EA 1 and 2. EPMA analyses of MMap reveal small variations of major elements: 54.8-55.7 wt% CaO and 42.1-43.1 wt% P_2O_5. All analysed samples are fluorapatite with ~ 3.3-3.5 wt% F and ≤ 0.01 wt% Cl. Minor concentrations of SiO_2 are detected in the range of 0.26-0.68 wt%, increasing from inner BSE-dark to outer BSE-lighter zones. The concentration of SrO is uniform in the range of 0.12-0.13 wt%, Na_2O varies from 0.04 to 0.06 wt%, and internal zones in general contain more Na_2O than outer zones. These results agree with data for MMap from YANG et al. (2014). The MMap contains trace amounts of U (7-24 ppm), Th (26-138 ppm), and Pb (2-6 ppm). These data are in agreement with our ID-TIMS results (Table 2) and with previous studies (YANG et al., 2014; CHEW et al., 2016); however, our analyses show higher concentrations of REE and Y (Table EA 2). The distributions of REE in the two analysed MMap grains are significantly different. One grain exhibits a smooth distribution of REE with subtle negative Ce and Eu anomalies, while another shows strong positive Eu anomaly (Eu/Eu* = 2.9-3.4) and negative Ce anomalies (Ce/Ce* = 0.74-0.77), indicating that apatite crystallized under a range of oxidizing conditions (CAO et al., 2012; PAN et al., 2016).

The chemical composition of CM and OBM apatite is more complex. BSE-dark CM (Fig. 2C) and OBM (Fig. 2F) apatite grains are characterized by the following concentrations of major and minor elements: 52.7-54.3 wt% CaO, 39.3-41.9 wt% P_2O_5, 0.6-1.4 wt% SiO_2. The darker domains have higher concentrations of CaO and P_2O_5 and lower content of SiO_2 than the lighter domains. All of the BSE-dark apatite domains are fluorapatite with 3.5-3.9 wt% F

and 0.05-0.09 wt% Cl, and contain minor concentrations of 0.08-0.17 wt% Na_2O, 0.03-0.06 wt% SrO, 0.54-1.18 wt% Y_2O_3, 0.002-0.048 wt% ThO_2, and 0.13-0.37 wt% La_2O_3.

The BSE-light areas have lower concentrations of major elements and higher concentrations of minor and trace elements: 50.4-52.0 wt% CaO, 37.4-39.4 wt% P_2O_5, 1.1-2.4 wt% SiO_2, 0.14-0.33 wt% Na_2O, 0.02-0.05 wt% SrO. All BSE-light domains also are fluorapatite with 3.5-3.8 wt% F but have higher Cl concentrations of 0.10-0.15 wt%. Also, BSE-light grains are enriched in Th, Y and REE relative to BSE-dark domains (0.063-0.143 wt% ThO_2, 1.01-1.80 wt% Y_2O_3, and 0.55-0.96 wt% La_2O_3). However, our LA-ICPMS analysis did not reveal any significant differences in trace element compositions between dark and light areas. LA-ICPMS data for concentrations of U (151-192 ppm), Th (512-1200 ppm), and Pb (40-127 ppm) are in general agreement with our ID-TIMS data (Table 2).

Both CM and OBM apatite have similar REE concentrations and distribution patterns (see Table EA 2). They are enriched in light REE (La-Nd) and have strong negative Eu-anomaly (Eu/Eu* = 0.22-0.25 for CM and 0.28-0.33 for OBM), indicating that these apatite crystallised under reduced conditions (CAO et al., 2012; PAN et al., 2016).

To better understand elemental distribution in CM and OBM apatite, we performed EPMA mapping of four minor elements (Si, Th, Sr, and Y, Fig. 4) because these elements can provide information about U (which was mostly below of detection limits) and REE distribution within individual apatite grains. Mapping of BSE-dark and BSE-light CM apatite (Fig. 4A) confirms that dark domains contain less Th, Si, and Y, but Sr concentration is identical in both (dark and light) areas. Unzoned areas show micron-scale heterogeneous distributions of minor elements; in one grain from CM (Fig. 4B) and OBM apatite (Fig. 4D) mapping reveals micron-wide strips enriched with Si. In one OBM grain all mapped elements except Sr have shown homogeneous distribution (Fig. 4C).

4.3. ID-TIMS results

Results of ID-TIMS U-Pb dating of apatite samples from Cheever mine, Old Bed mine, and McClure Mountains syenite are presented in Table 2.

4.3.1. Cheever mine (CM) apatite

Fourteen single apatite grains from the Cheever mine contain 93-275 ppm U and highly radiogenic Pb ($^{206}Pb/^{204}Pb$ between 2400-4300). These grains yielded a $^{206}Pb/^{204}Pb$ vs. $^{238}U/^{204}Pb$ errorchron age of 908 ± 23 Ma, and a $^{207}Pb/^{204}Pb$ vs. $^{235}U/^{204}Pb$ errorchron age of

908 ± 24 Ma. These regressions show considerable dispersion of the data (MSWDs 35-36) caused by documented within-grain heterogeneity and possible presence of tiny monazite inclusions (Fig. 2, 3, and 4). Both errorchrons provide an imprecise radiogenic composition of initial Pb of $^{206}Pb/^{204}Pb$ = 333 ± 78 and $^{207}Pb/^{204}Pb$ = 48.7 ± 8.3 (Fig. 5A and 5B).

A $^{207}Pb/^{206}Pb$ vs. $^{238}U/^{206}Pb$ T-W errorchron with MSWD of 29 and Y-axis intercept of 0.1491 ± 0.0099 yielded a lower intercept age of 912 ± 17 Ma. The low Y-axis intercept value indicates the radiogenic composition of initial Pb. The total Pb/U isochron (LUDWIG, 1998) yields a slightly more precise date of 907 ± 14 Ma (MSWD = 20) and an initial Pb compositions of $^{206}Pb/^{204}Pb$ = 339 ± 48 and $^{207}Pb/^{204}Pb$ = 49.6 ± 4.7 (Fig. 5C). The composition of initial lead from the total Pb/U isochron is also radiogenic and agrees with compositions obtained from the ^{238}U-^{206}Pb and ^{235}U-^{207}Pb isochrons but is more precise.

4.3.2. Old Bed mine (OBM) apatite

Sixteen apatite grains of Old Bed Mine apatite contain 133-342 ppm U; $^{206}Pb/^{204}Pb$ have a range of 1300-3600. These grains yielded results broadly similar to those from Cheever mine apatite but with a somewhat greater scattering in the isochron plots. Fourteen (of 16) analyses yielded a $^{206}Pb/^{204}Pb$ vs. $^{238}U/^{204}Pb$ errorchron date of 923 ± 20 Ma and $^{207}Pb/^{204}Pb$ vs. $^{235}U/^{204}Pb$ errorchron date of 924 ± 21 Ma; these regressions also show considerable data dispersion that significantly exceeds analytical uncertainties (MSWD = 1078-1093, Fig. 6A and B). The very large MSWD values are possibly related to heterogeneous compositions of apatite grains and monazite inclusions. The initial $^{206}Pb/^{204}Pb$ = 162 ± 39 and $^{207}Pb/^{204}Pb$ = 30.5 ± 4.4 obtained from the isochrons are slightly lower than in the Cheever Mine apatite but still very radiogenic compared to initial Pb found in most terrestrial rocks. BSE and EPMA revealed (Figs. 2C and 4A) that radiogenic composition of initial Pb caused by later generation(s) of high-U overgrowth.

A $^{207}Pb/^{206}Pb$ vs. $^{238}U/^{206}Pb$ T-W errorchron with very large MSWD value of 665 and Y-axis intercept of 0.186 ± 0.018 yielded a lower intercept date of 920 ± 19. The total Pb/U isochron with high MSWD of 547 yielded a date of 924 ± 13 Ma and initial Pb compositions of $^{206}Pb/^{204}Pb$ = 164 ± 26 and $^{207}Pb/^{204}Pb$ = 31.1 ± 2.7 (Fig. 6C).

Note that the ID-TIMS results of OBM apatite have smaller uncertainties than data from CM apatite (Fig. 5 and 6). The uncertainties in $^{206}Pb/^{204}Pb$ and $^{238}U/^{204}Pb$ are negatively correlated with the amount of ^{204}Pb and positively correlated with the procedural blank uncertainty.

4.3.3. McClure Mountain apatite (MMap)

Apatite grains from the McClure Mountain syenite have much lower U concentrations (6-15 ppm) and less radiogenic Pb ($^{206}Pb/^{204}Pb$ between 48-167) compared to CM and OBM apatite. Our MMap analyses, however, yielded more radiogenic Pb-isotopic ratios with $^{206}Pb/^{204}Pb$ of 48-167, higher than the data of SCHOENE AND BOWRING (2006) who reported $^{206}Pb/^{204}Pb$ ratios of 44-60. Six fractions of three grains each and 14 analyses of individual grains yielded a $^{206}Pb/^{204}Pb$ vs. $^{238}U/^{204}Pb$ errorchron age of 524.3 ± 2.7 Ma (MSWD = 125) and a $^{207}Pb/^{204}Pb$ vs. $^{235}U/^{204}Pb$ errorchron age of 525.5 ± 3.6 Ma (MSWD = 9.8) with a more "normal" composition of initial Pb of $^{206}Pb/^{204}Pb$ = 17.92 ± 0.30 and $^{207}Pb/^{204}Pb$ = 15.547 ± 0.034 (Fig. 7A and B).

For T-W and a total Pb/U diagrams, two outliers from our data were excluded (A149 02 and A149 06). The results of analytical sessions A149 and A151 yield a T-W errorchron (MSWD = 146) with Y-axis intercept of 0.870 ± 0.013 and lower intercept age of 524.6 ± 2.7 Ma; the total Pb/U errorchron yields the age of 524.6 ± 1.9 Ma with MSWD = 76 and the composition of initial Pb of $^{206}Pb/^{204}Pb$ = 17.88 ± 0.20 and $^{207}Pb/^{204}Pb$ = 15.55 ± 0.04.

Combining our data with analyses from (SCHOENE AND BOWRING, 2006) yields a 25-point T-W errorchron (MSWD = 87), Y-axis intercept of 0.874 ± 0.010, and lower intercept age of 524.9 ± 2.2 Ma. These pooled data yield the total Pb/U errorchron age of 525.3 ± 1.7 Ma (MSWD = 70) and the initial Pb compositions of $^{206}Pb/^{204}Pb$ = 17.78 ± 0.18 and $^{207}Pb/^{204}Pb$ = 15.54 ± 0.04 (Fig. 7C). This age and the isotopic composition of initial Pb are in agreement within uncertainties with previous results (SCHOENE AND BOWRING, 2006). High MSWD value indicates open U-Pb system behaviour and/or heterogeneous composition of initial Pb.

4.4. SHRIMP results

4.4.1. Old Bed Mine zircon

Zircon separated from the Old Bed Mine magnetite ore contains cores and rims, which were dated separately (Table 3, Fig. 8A and B). The U and Th concentrations in cores and rims range from 400 to 1351 ppm and from 48 to 244 ppm, respectively. The range of Th/U ratios is from 0.09 to 0.40 (Table 3). Seventeen spot analyses of zircon cores yield a Concordia age of 1008.0 ± 3.2 Ma (MSWD = 0.52) (Fig. 8C), which is close to the weighted average $^{207}Pb/^{206}Pb$ age of 1000.7 ± 4.2 Ma reported by VALLEY et al. (2009). Nine of 11 analyses of zircon rims yield a weighted mean $^{206}Pb/^{238}U$ age of 992.4 ± 7.7 Ma (Fig. 8D), which is younger and beyond uncertainties of the Concordia age for zircon cores. Two spot analyses treated as outliers in the weighted mean calculations have nearly concordant (Fig. 8D)

younger $^{206}Pb/^{238}U$ ages of 935 ± 15 and 915 ± 17 Ma (Table 3). These two analyses may indicate multiple zircon growth events.

4.4.2. Old Bed Mine apatite

In comparison with the OBM zircon, the OBM apatite separated from the same rock sample has much lower U concentrations (23 to 108 ppm), higher Th concentrations (172 to 680 ppm), and higher Th/U of 2.9 to 15.1 (Table 4). The SHRIMP data, corrected assuming a 1 Ga S-K model common Pb composition (Table 4), yield a nearly concordant compact cluster with a $^{206}Pb/^{238}U$ weighted average age of 1007 ± 21 Ma (Fig. 9A). Although this age estimate agrees with the OBM zircon age, it is significantly older than the errorchron ID-TIMS age of 924 ± 13 Ma for this apatite. However, data uncorrected for initial Pb show a spread of values on the T-W plot (Fig. 9B) allowing for calculation of a 958 ± 58 Ma lower-intercept age. This rather imprecise value is within error of the ID-TIMS results for this apatite. The isochron Y-axis intercept of 0.180 ± 0.030 (within error of the ID-TIMS Y-axis intercept of 0.186 ± 0.018) supports the interpretation that the initial Pb isotopic composition is radiogenic. Therefore, use of the S-K value for 1.0 Ga common Pb is inappropriate.

4.5. LA-ICPMS results

4.5.1. MMap, MAD, and Durango apatite

Analyses of apatite by LA-ICPMS used McClure Mountain apatite as a primary matrix-matched reference. Although it is impossible to evaluate the accuracy of a primary reference material age from the LA-ICPMS analyses, the most important quality of the reference, its age homogeneity, can be evaluated from the within-session variability of ages calculated using self-normalised U/Pb ratios (as described in section 3.2.1). The MMap analysed in 37 LA-ICPMS analytical sessions as a primary matrix-matched RM showed a range of median U concentrations (median values for a set of spot analyses in each session) from 10.6 to 29.4 ppm (Table EA 3). The within-session 2SE (standard errors) uncertainties of calculated lower-intercept unconstrained T-W isochron ages using self-normalised $^{238}U/^{206}Pb$ ratios ranged from ± 1.1 % to ± 5.2 %,with an average value of ± 2.2 %. This relatively large uncertainty may be caused by a poor counting statistics due to a small laser spot that was limited by the small grain size of this apatite and relatively low U concentrations, and/or by age or initial Pb heterogeneity of this material. The relatively large MMap age uncertainty in each session is then propagated to the age uncertainty of unknowns.

The MAD1 apatite (486.58 ± 0.85 Ma, ID-TIMS, THOMSON et al., 2012) treated as an unknown in 10 sessions using MMap as a primary matrix-matched reference (Table EA 4) showed a range of median U concentrations (one median value per session) from 33.8 to 48.6 ppm. The average age value of 484.1 ± 10.2 Ma (2SD of ± 2.1%, MSWD = 3.6) Ma for lower-intercept ages of anchored T-W isochrons is within uncertainty with the published ID-TIMS results (THOMSON et al., 2012) for this apatite.

The MAD2 apatite (474.25 ± 0.41 Ma-old, ID-TIMS, THOMSON et al., 2012) treated as an unknown in 28 LA-ICPMS analytical sessions using MMap as a primary matrix-matched reference (Table EA 4) yielded a range of median U concentrations from 27.7 to 57.8 ppm (one median value per session), essentially overlapping the range observed in MAD1. The average age value of 470.3 ± 10.1 Ma (2SD of ± 2.1%, MSWD = 3.9) for lower-intercept ages of anchored T-W isochrons is within uncertainty with the published ID-TIMS results (THOMSON et al., 2012) for this apatite. The relatively large uncertanty of the age is caused by the propagated elevated uncertainty in the MMap matrix-matched RM data. For this apatite we also calculated F values based on its Iolite $^{238}U/^{206}Pb$ ratios and a known ID-TIMS age of this material. Then these F values were used to calculate self-normalised ages for this apatite. Average within-session uncertainty for the MAD2 self-normalised ages is ± 1.2 %, which is 1.8 times smaller than for the self-normalised ages of the MMap RM .

Analyses of Durango apatite in four analytical sessions (Table EA 4) resulted in an average age value of 31.8 ± 1.5 Ma (2SD, MSWD = 1.2), within uncertainty of its accepted age value of 31.44 ± 0.18 Ma (MCDOWELL et al., 2005).

4.5.2. Cheever mine (CM) and Old Bed mine (OBM) apatites

Uranium and Th concentrations are quite variable in CM and OBM apatite samples and range from tens to thousands of ppm (Table EA 5 and EA 6). Thorium concentrations are higher than U in both high- and low-U samples and Th/U ranges from 1.3 to 7.1. Uranium concentrations in in OBM and CM apatites are significantly higher than in McClure Mountain apatite, which lies in the range of 11-29 ppm (Table EA 3). However, relatively low U concentrations (4.8-106 ppm) were observed in two CM and OBM analytical sessions (T8183 and T8400, Table EA 5) where it was possible to use MMap as a matrix-matched RM. LA-ICPMS data for atypically low-U (4.8 to 69.6 ppm) Cheever mine apatite form a T-W isochron (after rejecting one outlier, Fig. 10) with a lower intercept age of 907 ± 15 Ma (MSWD = 2.5), within uncertainty of the ID-TIMS total Pb/U isochron age of 907 ± 14 Ma,

MSWD = 20). The Y-axis intercept of this unconstrained isochron is 0.728 ± 0.086. This shows that the low-U domains have much less radiogenic composition of initial Pb than that derived from the ID-TIMS data and explains large MSWD values of ID-TIMS results.

The MMap was also used as a primary RM in analytical session T8400 with low-U OBM apatite. A lower-intercept T-W isochron age of 897 ± 27 Ma (Fig. 11A, Table EA 5) obtained in this session is within uncertainty of the ID-TIMS age for this apatite. A limited spread of the data points did not allow an unconstrained isochron calculation and the regression was anchored to the Y-axis intercept of 0.186 ± 0.018 (value from the ID-TIMS data). In another analytical session (T6753, Table EA 5) MMap normalisation was applied to the OBM apatite with more typical U concentrations (Fig. 11B) and resulted in an unconstrained T-W isochron lower intercept age of 878 ± 48 Ma. A Y-axis intercept on this isochron is 0.178 ± 0.041, which is within uncertainties of the ID-TIMS estimate for the radiogenic initial $^{207}Pb/^{206}Pb$ in this sample. The OBM analyses with high U concentrations (> 310 ppm) were excluded from the regression because the relatively large laser beam size that was used for obtaining sufficient counting statistics for the ^{238}U signal in the MMap primary matrix-matched reference, gave ^{238}U signal that exceeded $1.6x10^6$ cps for OBM spot analyses. This very high count rate exceeds a cut-off for the LA-ICPMS SEM measurements. This example emphasizes the need for standards and unknowns to have similar U concentration for performing analyses under the same run conditions, leading to the conclusion that MMap reference material should be used with caution for high-U apatite unknowns.

In analytical session T8184 (Table EA 5) we observed typical high U concentrations (300-500 ppm) for CM apatite, which allows to use the OBM ID-TIMS results as a primary RM. The data form a compact, nearly concordant cluster (Fig. 12); an anchored T-W isochron defines a lower intercept age of 941 ± 46 Ma (within uncertainty of the ID-TIMS age). The anchoring used the initial $^{207}Pb/^{206}Pb$ value for this apatite of 0.1491 ± 0.0099, as determined by ID-TIMS. Use of the S-K model for initial Pb correction results in a much older age estimate of 1029.1 ± 7.9 Ma. Although this value is more precise, it is less accurate compared to the ID-TIMS results. The significant difference in precision between these two values is caused by the higher position of the S-K anchoring point ($^{207}Pb/^{206}Pb$ = 0.9021), which makes the uncertainty envelope narrower.

5. Discussion

5.1. Correction for initial Pb

Apatite may incorporate significant amounts of Pb (referred to as initial lead) during crystallization due to similar ionic radii of Pb and Ca (e.g., WHITTAKER AND MUNTUS, 1970), and the isotopic composition of initial Pb is required for accurate determination of the age of a mineral. Several approaches to calculate the isotopic composition of initial Pb include: 1) choosing a composition based on one of the models of Pb isotopic evolution in the continental crust (e.g., STACEY AND KRAMERS, 1975); 2) determining the Pb isotopic composition of a cogenetic low-U mineral, such as K-feldspar, plagioclase, or low-U calcite, where Pb^{2+} can replace K^{+} or Ca^{+2} (CHAMBERLAIN AND BOWRING, 2001; Amelin and Zaitsev, 2002); 3) using initial-Pb-uncorrected data to construct two-dimensional T-W or three-dimensional linear total Pb/U isochron (LUDWIG, 1998) for calculating ages of cogenetic samples assumed to have the same initial Pb isotopic composition.

Our observations (Figs. 2, 4) and data from LUPULESCU et al. (2017) reveal multiple generations of apatite with variable compositions, as well as metasomatic reworking of different degrees with formation of monazite inclusions (Fig. 3). It is possible that each zone has its own composition of initial Pb as was observed for the low-U CM apatite, which has a much less radiogenic initial Pb isotopic composition (Fig. 10) compared to the high-U varieties of this apatite. These textural observations suggest that several conditions of the isochron model could have been violated, including open system behaviour, the presence of multiple domains with different ages and isotopic compositions of initial Pb, and inclusions of monazite (and in some cases of magnetite and zircon).

The OBM and CM ore samples do not contain minerals with low μ-value ($^{238}U/^{204}Pb$) so in this study we applied a correction for initial Pb isotopic composition from the total Pb/U regression (Fig. 5 and 6), and S-K model. To compare the effects of the correction method for the apatite analysed here, we plotted data corrected for initial-Pb in a conventional (Wetherill-type) Concordia diagram that most commonly used in U-Pb dating for presenting radiogenic isotope ratios (Fig. 13).

The S-K model isotopic compositions of initial Pb and those obtained by the three-dimensional-total isochron are the same within uncertainties for sample MMap. The U-Pb data corrected for the three-dimensional-total isochron and the S-K model initial Pb values form almost indistinguishable clusters in Concordia diagrams (Fig. 13A and B). The data corrected using the total U/Pb isochron initial Pb yield a Concordia age of 525.10 ± 0.75 Ma (MSWD = 1.1), which is within uncertainty of the S-K model–corrected Concordia age of

524.13 ± 0.69 Ma (MSWD = 5.1). Because the age based on the total Pb/U isochron is free from assumptions about the isotopic composition of initial Pb, we consider the total Pb/U isochron age being more accurate than the age obtained using the S-K initial Pb correction. Our single Concordia age is not within uncertainties of the zircon $^{207}Pb/^{235}U$ age of 523.98 ± 0.12 Ma (SCHOENE AND BOWRING, 2006), which was interpreted as the crystallization age. This small disagreement possibly reflects different crystallization times of zircon and apatite.

The importance of an accurate correction for the initial Pb is clearly demonstrated for the CM and OBM apatite. Data corrected for the S-K model show normal age discordance and a substantial spread of the Pb/U along the Discordia line (Fig. 13D and F). The data corrected using the S-K model initial Pb form an array with $^{207}Pb/^{235}U$ ages ranging from ~ 970 to 1030 Ma and from ~ 960 to 1040 Ma for CM and OBM apatite, respectively. Both age ranges are significantly older than the 907 ± 14 and 924 ± 13 Ma ages obtained from the total Pb/U isochrons. The $^{206}Pb/^{238}U$ and $^{207}Pb/^{235}U$ data corrected for initial Pb isotopic compositions obtained from the total Pb/U isochrons are concordant but have large uncertainties because of significant uncertainties of calculated initial $^{206}Pb/^{204}Pb$ and $^{207}Pb/^{204}Pb$ ratios. The CM apatite $^{207}Pb/^{235}U$ ages are in the range of 930-960 Ma, while OBM apatite $^{207}Pb/^{235}U$ ages are in the range of 900-940 Ma (Fig. 13C and E). Concordia plots for OBM and CM apatites illustrate the significant difference between the two approaches of initial Pb correction. Thus, the apatite samples likely experienced open U-Pb system behaviour and/or have heterogeneous isotopic composition of initial Pb.

Deviations from the isochron model assumptions are identifiable only by high-precision ID-TIMS results. It is impossible to determine if an incorrect initial Pb composition was used where lower precision *in situ* SHRIMP and LA-ICPMS data form compact clusters of discordant data points that do not allow for the T-W isochron age calculations. In these cases, reliance on anchoring of a T-W isochron to an assumed Y-axis intercept may result in significantly biased age estimates. This possibility is clearly demonstrated by the CM and OBM apatite results, where inappropriate application of S-K correction may cause up to 10% age bias.

5.2. The effect of ^{230}Th disequilibrium

The high Th/U (up to 15, Table 4) in OBM apatite suggests chemical fractionation of Th from U during apatite crystallization and therefore a possible enrichment in ^{230}Th causing excess of ^{206}Pb and older $^{206}Pb/^{238}U$ ages (SCHÄRER, 1984; PARRISH, 1990, Amelin and

Zaitsev 2002). In our case, $^{207}Pb/^{235}U$ and $^{206}Pb/^{238}U$ ages for OBM and CM apatite are concordant within their large uncertainties, indicating that the contribution of ^{230}Th on excess ^{206}Pb is insignificant compared to the other sources of uncertainty.

5.3. McClure Mountain apatite as a reference material for *in situ* analysis

McClure apatite has good age homogeneity, and its age is precisely known from consistent results of two ID-TIMS studies, but the relatively low U concentrations (10-30 ppm), and small grain size of MMap that limit the laser or primary ion beam size, result in reduced ion counting statistics and hence an increased age uncertainty as shown in the section 4.3.1. This apatite is suitable as primary reference material for dating of apatite unknowns with similar low U content and "normal" S-K model compositions of initial Pb, which is typical for most apatite samples (O'SULLIVAN et al., 2020).

5.4. Old Bed mine apatite as a potential reference material for *in situ* analysis of high-U samples

MAO et al. (2016) and O'SULLIVAN et al. (2020) have shown that apatite in the most cases is a low-U mineral (< 30 ppm). MAO et al. (2016) reported only one case of high-U apatite (681 ppm) from Omineca alkali-feldspar syenite, British Columbia, Canada. There are, however, more occurrences of high-U apatite in alkaline rocks which might need high-U RMs to be dated by *in situ* techniques.

YU et al. (2019) reported chemical composition of hydrothermal apatite in Zoujiashan uranium deposit, China, which contains U in the range of 1350-2970 ppm, formed during several growth episodes and marks different stages of ore deposition. Deciphering evolution of ore fluid(s) and ore deposition chronology therefore requires precision and accurate *in situ* dating with high-U apatite RMs.

NEYMARK et al. (2019) described high-U apatite (up to 1.5% U) from Coles Hill uranium deposit, USA. This apatite is closely related to U mineralization; precise and accurate chronology of the apatite is therefore critical for understanding genesis of the deposit.

VERÍSSIMO et al. (2016) described two generations of apatite in the Itataia phosphate-uranium deposit, Brazil. The first generation has low U contents (in the range of 2-34 ppm) whereas the second generation of U-bearing apatite has elevated U concentrations of 29-314 ppm.

Journal Pre-proof

BROS et al. (1996) reported U contents of 177-237 ppm for apatite from Oklo uranium deposit in Gabon that hosts the famous natural nuclear reactors. Apatite in the deposit is of hydrothermal origin induced by a temperature increase due to the nuclear reactions and therefore marks the inception of this unique process.

KROGSTAD AND WALKER (1994) reported U-Pb systematics of apatite with U content in the range of 142-1224 ppm in the Tin Mountain pegmatite, South Dakota, USA. Zircon from pegmatite is usually metamict because it contains thousands of ppm U (e.g., WANG et al., 2007; ADETUNJI et al., 2016; SHAW et al., 2016), while apatite is not prone to metamictisation due to very efficient self-annealing of α decay (Oelkers and Montel, 2008; Li et al., 2017) . *In situ* U-Pb dating of such high-U apatite can potentially provide more reliable chronological constraints on crystallization processes than zircon or other high-U and metamict minerals like columbite-tantalite (SMITH et al., 2004).

Another possible application is dating of sedimentation and diagenesis processes. MILLER et al. (1989) studied U-Pb systematics of fluorapatite cementing conglomerate-sandstone in the Thelon Formation, Canada, and reported elevated U concentrations in the range of 129-2227 ppm. High-quality *in situ* dating of such diagenetic processes require RMs with similar U concentration. Such diagenetic apatite is a common cement in Proterozoic fluvial sandstone basins and U-Pb geochronology can help to constrain timing of sedimentation (MILLER et al., 1989 and references therein).

These examples illustrate that we can expect finding apatite with high-U content in U-rich systems such as pegmatites, felsic and alkali rocks, and U deposits of different types. U-Pb systematics of apatite in these geological settings can provide chronological constraints on crystallization, ore formation, and sedimentation processes.

We conducted 17 LA-ICPMS analytical sessions where OBM was used as a primary matrix-matched reference and observed a range of median values for each session from 98.5 to 482 ppm U (Table EA 6). In the absence of another well-characterized high-U apatite, the quality of this reference material can be evaluated by calculating within-session age uncertainties based on self-normalized U/Pb ratios, as was described in section 4.3.1 for the MMap material. The lower intercept ages were calculated using T-W isochrons anchored to initial $^{207}Pb/^{206}Pb$ values determined by ID-TIMS. An average uncertainty (2SE) of the self-normalized ages is about ± 3.9 % (Table EA 6), which is significantly larger than for the MMap and MAD self-normalized age uncertainties. This elevated age uncertainty may be

caused by shallow slopes of the isochrons anchored to the very low initial $^{207}Pb/^{206}Pb$ value resulting in large uncertainties of the lower Concordia intercepts for nearly concordant clusters of spot analyses.

A weighted average age of these self-normalized data is 943.0 ± 5.5 Ma, which is 2.1 % older (even after eliminating 3 outliers with high age values) and is beyond uncertainty of the ID-TIMS age of 924 ± 13 Ma. A reason for this discrepancy is illustrated by the Fig. 14, which shows that the $F = (^{238}U/^{206}Pb_{true})/(^{238}U/^{206}Pb_{Iolite})$ correction factor F is grossly over-estimated in case of a T-W isochron with a very shallow slope (blue line constructed using radiogenic Y-axis intercept). In this figure $R_t = {}^{238}U/^{206}Pb_{true}$ and $r_{b2} = {}^{238}U/^{206}Pb$ derived from the lower intercept of the anchored to $^{207}Pb/^{206}Pb_{ini}$ = 0.186 ± 0.018 T-W isochron age for NIST-normalised ("raw") $^{238}U/^{206}Pb$ ratios. In fact, the calculated R_{b2} $^{238}U/^{206}Pb$ ratio should be used instead of r_{b2} to evaluate the actual instrumental bias in the measured U/Pb ratios. The R_{b2} value can be calculated from the y = ax + b equation of the T-W isochron obtained using the "other X_Y (-Z) plot" option in Isoplot for $y = {}^{207}Pb/^{206}Pb$ for the true apatite age. The same data set would give a significantly different F value if the S-K Y-axis intercept is used for anchoring of the T-W isochron (green line in Fig. 14). This isochron has a much steeper slope and the difference between the r_{b1} and R_{b1} ratios that one would use for the F factor calculation is essentially negligible in this case.

The age effect of the difference between the two anchoring methods used for calculating the F factors can be illustrated by the NIST-normalised ("raw") data for the low-U OBM apatite. The "raw age" for this data set in case of anchoring to the S-K Y-axis intercept is 906 ± 10 Ma. The "raw age" is 831 ± 37 Ma if the T-W isochron is anchored to the $^{207}Pb/^{206}Pb_{ini}$ = 0.186 ± 0.018 determined by TIMS. F factors calculated from these biased ages are also significantly different (0.939 ± 0.064 and 0.881 ± 0.064 , respectively, Table EA 5). Using these different F values we obtain self-corrected OBM ages of 1007 ± 23 and 928 ± 26 Ma, respectively. These ages differ by 8.5% due to grossly overestimated matrix effects correction when the $F = R_t/r_{b2}$ correction factor is applied. For the F value calculated as R_t/R_{b2} the age of 928 ± 26 Ma is within uncertainty of the OBM apatite age dermined by ID-TIMS, as it is expected for the self-normalised U/Pb ratios.

5.5. The advantages of using Old Bed mine apatite as a reference material for quadrupole LA-ICPMS

In situ dating of apatite is commonly performed using laser ablation ICPMS with quadrupole mass analyser (LA-Q-ICPMS), a widely available type of isotope mass spectrometer. However, quadrupole mass spectrometers have lower sensitivity than sector field mass spectrometers under similar operating conditions (VANHAECKE, 2012), hence larger size of the laser spot is necessary to achieve similar intensity of the ion beam. In LA-ICPMS U-Pb chronology of zircon, the diameter of the laser spot required for achieving relatively high precision is usually ~20 µm for quadrupole and sector field mass analysers (SYLVESTER AND JACKSON, 2016). For apatite, which commonly has lower U concentrations than zircon, the diameter of the laser spot should be larger to provide sufficient ion counts.

Fine grained MMap, which has low U concentrations, has been used successfully as a primary RM in recent LA-Q-ICPMS analyses (e.g. KIRKLAND et al., 2018). However, we argue that this matrix-matched RM is not optimal for analyses of high-U apatite unknowns. The OBM apatite from the Adirondacks IOA deposit has a larger grain size and ~14 times higher median U concentration than MMap (161 ppm and 12.3 ppm, respectively, based on the data in tables EA3-EA5), and its use as an RM in apatite U-Pb dating with LA-Q-ICPMS should yield a substantial improvement in the age precision. The relative uncertainty component related to counting statistics in LA-ICPMS dating can be approximated by a quadratic sum of counting statistics relative uncertainties of the unknown and the RM. Considering an unknown apatite with U concentration similar to that of OBM, and the total number of accumulated counts for ^{238}U of 10^5, a $\sqrt{n}$ counting uncertainty for the unknown corresponding to the relative uncertainty of 0.316 %. If we use MMap as an RM, we get 14 times lower number of counts for the same isotope, and the corresponding relative uncertainty of 1.18 %. This yields a total relative uncertainty of $(0.316^2 + 1.18^2)^{0.5} = 1.22$ %, which is dominated by the uncertainty of the RM measurement. On the other hand, if we use OBM as an RM, the total uncertainty would be $(0.316^2 + 0.316^2)^{0.5} = 0.45$ %, or ca. 2.7 times lower than when using MMap as an RM. The gain in precision can be even larger for unknowns with larger homogeneous grains where the spot size is currently limited by the grain size if using MMap, but using OBM as an RM would allow an increase in the beam size and hence improve counting statistics and precision. CHEW et al. (2019) have shown that the spot size for RMs should be adjusted carefully for optimum intensity and not to exceed the pulse-analogue threshold because it may result in measurements in analogue mode that potentially involves additional systematic uncertainties. Alternatively, using a high-uranium

RM such as OBM would enable analysis of heterogeneous samples with a smaller laser beam and still achieve acceptable precision.

5.6. Timing of radiogenic Pb accumulation and application of U-Pb systematics of CM and OBM apatites to Adirondacks IOA deposits

The time needed to produce the radiogenic composition of initial Pb observed in samples CM and OBM apatites can be calculated using their initial Pb isotopic compositions estimated by 3D Total Pb/U isochron. The modelling is based on the following assumptions: (1) both apatite samples crystallized at the same time (T_1 = 915 Ma), which is true for each apatite within their age uncertainties; (2) both apatite samples originated from the same source that experienced significant U enrichment at some time T_0 in the past; (3) the difference in initial $^{206}Pb/^{204}Pb$ and $^{207}Pb/^{204}Pb$ between CM and OBM apatite is caused by the difference in μ-value which appeared at T_0 and remained unchanged until crystallization time T_1. As we have shown above, the apatite has radiogenic and most likely heterogeneous compositions of initial Pb; (4) U-Pb isotopic system remained closed since the apatite crystallized at T_1.

We can construct a paleo-isochron which passes through the initial $^{206}Pb/^{204}Pb$ and $^{207}Pb/^{204}Pb$ compositions of two apatite samples. The slope of this two-point fossil isochron is 0.1057, while its uncertainty strongly depends on the error correlation of the initial Pb-isotope compositions. Assuming the error correlation of 0.99 we get the slope uncertainty of ± 0.0049 (Fig. 15). The error correlations of 0.95 and 0.90 yield larger slope uncertainties of ± 0.010 and ± 0.014, respectively.

Using the slope of the paleo-isochron and the crystallization age of 915 Ma, T_0 (time of the crystallization of high-μ minerals) can be determined by numeric modelling of Pb isotope evolution between T_0 and T_1. The modelling (Table EA 7) yields the time of 1085^{+105}_{-112} Ma before the apatite crystallization with μ-values of 10,386 and 4,713 for CM and OBM apatite, respectively. This date is within uncertainty of primary ore crystallization (Fig. 8) and suggests that the radiogenic composition of initial lead in Cheever mine and Old Bed mine apatite was derived from the dissolution and reprecipitation of U-Th-rich minerals with high $^{206}Pb/^{204}Pb$, $^{207}Pb/^{204}Pb$, and μ. The nature of this U-Th-rich precursor of the apatites is uncertain. REGAN et al. (2019) described two types of monazite, which were formed at the expense of fluorapatite (type 1) and britholite (type 2) due to dissolution-reprecipitation reactions, possibly with NaCl fluid. These authors suggested that further increase of Ca concentration leads to the consumption of monazite and formation of allanite and

fluorapatite, similar to reactions described by FINGER et al. (1998). In our case, a more likely scenario is the dissolution-reprecipitation of primary apatite. It has been shown that apatite recrystallization can occur during amphibolite to granulite facies metamorphism (BINGEN et al., 1996) at a temperature of less than 150°C (ROMER, 1996). If crystal growth occurs by replacing a precursor phase it can incorporate a specific type of initial Pb – inherited Pb (SMYE et al., 2018), with isotopic composition that depends on the chemical composition and the age of the precursor mineral. Such inherited radiogenic composition of initial Pb have been described for titanite (ZHANG AND SCHÄRER, 1996; ROMER AND RÖTZLER, 2003).

The median of measured μ-values in CM apatite (~22,000) is about two times greater than in the OBM apatite (~12,000), which correlates with more radiogenic initial Pb isotopic composition in this sample. This could be explained by the proximity of newly formed apatite to the source of the fluid, i.e. the dissolution-reprecipitation process occurred at very short distances and in fact, may have been just precipitation of redissolved apatite with preservation and partial homogenization of previously accumulated radiogenic Pb. For example, extremely "abnormal" initial Pb isotopic compositions with $^{207}Pb/^{206}Pb_{ini} < 0.005$ were observed in apatite from metasomatites in the Coles Hill U deposit, VA, USA (Neymark et al., 2019). However, these abnormal values were observed only in apatite at the immediate proximity (within several μm) to the uranium mineralization (source of ^{222}Rn-produced excess ^{206}Pb), but not in apatite from non-mineralized rocks.

Combining all of the geochronological data, we propose the following model for IOA deposits of Adirondack Mountains (Fig. 16): 1) formation of ores at 1040-1008 Ma, 2) formation of monazite at ~ 980 Ma due to Na-rich fluid, and 3) formation of apatite with radiogenic Pb composition by dissolution-reprecipitation of U-Th-rich minerals at ~ 920-910 Ma.

5.7. The role of apatite in deciphering geological evolution of IOA systems

Recent investigations of apatite from IOA deposits in eastern Adirondack Mountains (LUPULESCU et al., 2017; TAYLOR et al., 2019) and the Pea Ridge magnetite deposit, MO, USA (MERCER et al., 2020), IOA deposits of Chilean iron belt (PALMA et al., 2019), tourmaline B and Sr isotope systematics from the giant Taocun IOA deposit, China (SU et al., 2019), trace element and oxygen isotopes study of magnetite from IOA Bafq deposit, Iran (GHAZI et al., 2019), have shown that the protracted formation of IOA deposits due to multiple hydrothermal pulses might be the common feature of IOA systems. For example,

detailed study of the ores from Pea Ridge IOA deposit reveals numerous monazite and xenotime inclusions in the fluorapatite, suggesting late metasomatic reworking (HARLOV et al., 2016). Geochronology of apatite and monazite inclusions (NEYMARK et al., 2016) have shown that metasomatic events occurred 5-30 m.y. after the primary ore formation. Such complex genesis is in agreement with a flotation model, which proposed a combination of magmatic and hydrothermal processes (KNIPPING et al., 2015; SIMON et al., 2018). Our study has also confirmed that apatite from IOA deposits of eastern Adirondack Mountains (particularly CM) crystallised from 2-3 fluid pulses with different chemical compositions. The first generations were low in Cl and Na contents, while the last episode had high concentrations of these elements. MERCER et al. (2020) mentioned that Na contents control the degree of REE-solubility and chloride should be the main REE-transporting ligand. The crystallization of this fluid led to formation of REE-rich apatite, where REE+Y was charged balanced by Si and Na: $Si^{4+} + (REE+Y)^{3+} = P^{5+} + Ca^{2+}$ and $Na^{+} + (REE+Y)^{3+} = 2Ca^{2+}$ (PAN AND FLEET, 2002; HARLOV et al., 2005).

Because trace element content and distribution (e.g., REE patterns, Sr/Y, U/Th, Sr/Mn ratios) allow determination of many parameters, such as fluid/melt composition, temperature, pressure, redox state, pH, it has been shown that many generations of apatite can form in IOA (and IOCG) systems. These episodes, from primary magmatic genesis to hydrothermal pulses, are responsible for dissolution/reprecipitation of previous generations of the mineral. Therefore, the optimal strategy for using apatite to elucidate geological history includes: (1) textural observations to help distinguish magmatic and subsequent metasomatic/hydrothermal apatite; (2) compositional data of each apatite generation to understand physicochemical conditions of magmatic and hydrothermal fluids; (3) *in situ* U-Pb dating to establish a temporal framework for each process. In addition, our research has shown that another important requirement is an accurate determination of initial Pb composition. As shown by our samples, it is possible that hydrothermal apatite could have a radiogenic composition of initial Pb, and for *in situ* dating of such phases, CM and OBM apatite could be used as matrix-matched standards, but with some caution.

6. Conclusions

High-precision ID-TIMS dating of apatite from the Cheever and Old Bed mines yielded total Pb/U errorchron ages of 907 ± 14 Ma (MSWD = 20) and 924 ± 13 Ma (MSWD = 547), respectively, and anomalously radiogenic compositions of initial Pb that suggest the

participation of high-μ fluid in the mineralization. The apatite ages are younger than the core and rim zircon SIMS U-Pb ages of 1008.0 ± 3.2 Ma and 992.4 ± 7.7 Ma from OBM ore, indicating protracted fluid activity in the IOA ore-forming system that lasted for ~100 Ma after the ore formation. All four types of U-Pb isochrons yield high MSWD value, probably due to intragrain heterogeneity and metasomatic alteration. The $^{206}Pb/^{238}U$ and $^{207}Pb/^{235}U$ ratios corrected for initial Pb fall on Concordia but this apparent concordance may be due to the large uncertainties of initial Pb composition inferred from the total Pb/U isochron, especially initial $^{206}Pb/^{204}Pb$. Although all of these features make these materials imperfect primary references, CM and OBM apatite samples can be used with caution as reference materials for *in situ* analysis of apatite with similarly high-U content and produce significant improvement in precision compared to low-U reference materials, until better behaved high-U apatite samples are found and characterised.

In situ methods (SHRIMP and LA-ICPMS), based on anchored isochrons using "normal" S-K model initial Pb composition, yielded apparent ages older than the ages determined by ID-TIMS for CM and OBM apatites. A word of caution here is that most of these spot analyses formed compact and near-concordant clusters that resulted in lower intercepts of anchored T-W isochrons that may be interpreted as real ages. Interpretation of such erroneous geochronological information would lead to incorrect geological models.

Determination of accurate initial Pb values is also relevant to the McClure Mountain apatite. This material has low $Pb_{radiogenic}/Pb_{initial}$ and therefore is susceptible to uncertainty in the initial Pb correction. Although the compositions inferred from the S-K model and total-Pb/U isochron are almost identical, small differences significantly change the accuracy and precision of the obtained age. Two independent ID-TIMS studies of MMap yielded identical ages and thus confirm that this apatite is usable as a reference material for *in situ* U-Pb isotopic analysis of apatite with low U/Pb, $Pb_{radiogenic}/Pb_{initial}$ and "normal" composition of initial Pb. Our data corrected for initial Pb using the total U/Pb isochron yield the single Concordia age of 525.10 ± 0.75 Ma (MSWD = 1.1). However, our LA-ICPMS results show that low U concentration and small grain sizes of this apatite cause an elevated uncertainty of ages calculated from self-normalised U/Pb ratios. Propagation of these uncertainties in the primary reference material increases uncertainties in the ages of unknowns.

Precise and accurate chronology, combined with trace element and REE data, provide valuable information for resolving of a wide range of geological problems. However, the lack

of well-documented reference materials with diverse compositions and stable U-Pb system compromises the ability of getting reliable data by high-productive *in situ* methods. Therefore, better materials with high-precision U-Th-Pb systematics are needed.

Acknowledgements

We gratefully acknowledge Michael Kunk (U.S. Geological Survey), Stuart Thomson (University of Arizona), and Marian Lupulescu (New York State Museum) for providing apatite samples for this study. We thank Sonja Zink (ANU) for the maintenance of SPIDE^{2}R lab and Vickie Bennett for her support. We thank Marc Norman (ANU) for his constructive informal internal review. The manuscript was officially reviewed by Gary O'Sullivan (University College Dublin) and two anonymous referees whose comments significantly improved this paper. We are also grateful to Dr. Balz Kamber, the Chemical Geology editor, who's thorough review and suggestions helped to straighten up our points. We thank Durgalakshmi (ANU) for her help with the mount preparation and BSE-imaging. The authors acknowledge the facilities and the scientific and technical assistance of Microscopy Australia at the Centre for Advanced Microscopy, ANU, a facility that is funded by the University and the Federal Government. We also thank Brett Knowles (ANU) for his assistance with LA-ICPMS trace elements analysis.

The authors thank Kate Souders and Richard Moscati (U.S. Geological Survey) for optimizing the LA-ICPMS system and sample preparation and imaging at the USGS Microbeam Laboratory in Denver, respectively. Any use of trade, firm, or product names is for descriptive purposes only and does not imply endorsement by the U.S. Government.

References

Adetunji, A., Olarewaju, V. O., Ocan, O. O., Ganev, V. Y., and Macheva, L., 2016. Geochemistry and U-Pb zircon geochronology of the pegmatites in Ede area, southwestern Nigeria: A newly discovered oldest Pan African rock in southwestern Nigeria. Journal of African Earth Sciences 115, 177-190.

Aleinikoff, J. N. and Walsh, G. J., 2016. Ages and origins of low-Ti magnetite deposits of the eastern Adirondacks: SHRIMP U-Pb and REE evidence from complexly zoned zircon. Geol. Soc. Amer. Abst. with Prog. 48. doi: 10.1130/abs/2016NE-272005.

Aleinikoff, J. N., Walsh, G. J., and McAleer, R. J., 2021. New interpretations of the ages and origins of the Hawkeye Granite Gneiss and Lyon Mountain Granite Gneiss, Adirondack Mountains, NY: Implications for the nature and timing of Mesoproterozoic plutonism, metamorphism, and deformation. Precambrian Research 358, 106112.

Amelin, Y., Koefoed, P., Iizuka, T., Fernandes, V. A., Huyskens, M. H., Yin, Q.-Z., and Irving, A. J., 2019. U-Pb, Rb-Sr and Ar-Ar systematics of the ungrouped achondrites Northwest Africa 6704 and Northwest Africa 6693. Geochimica et Cosmochimica Acta 245, 628-642.

Amelin, Y. and Zaitsev, A. N., 2002. Precise geochronology of phoscorites and carbonatites:: The critical role of U-series disequilibrium in age interpretations. Geochimica et Cosmochimica Acta 66, 2399-2419.

Andersson, S. S., Wagner, T., Jonsson, E., Fusswinkel, T., and Whitehouse, M. J., 2019. Apatite as a tracer of the source, chemistry and evolution of ore-forming fluids: The case of the Olserum-Djupedal REE-phosphate mineralisation, SE Sweden. Geochimica et Cosmochimica Acta 255, 163-187.

Ansberque, C., Mark, C., Caulfield, J. T., and Chew, D. M., 2019. Combined in-situ determination of halogen (F, Cl) content in igneous and detrital apatite by SEM-EDS and LA-Q-ICPMS: A potential new provenance tool. Chemical Geology 524, 406-420.

Armbrustmacher, T. J., 1984. Alkaline rock complexes in the Wet Mountains area, Custer and Fremont counties, ColoradoProfessional Paper.

Armbrustmacher, T. J. and Hedge, C. E., 1982. Genetic implications of minor-element and Sr-isotope geochemistry of alkaline rock complexes in the Wet Mountains area, Fremont and Custer counties, Colorado. Contributions to Mineralogy and Petrology 79, 424-435.

Barbarand, J., Carter, A., Wood, I., and Hurford, T., 2003. Compositional and structural control of fission-track annealing in apatite. Chemical Geology 198, 107-137.

Barfod, G. H., Krogstad, E. J., Frei, R., and Albarède, F., 2005. Lu-Hf and PbSL geochronology of apatites from Proterozoic terranes: A first look at Lu-Hf isotopic closure in metamorphic apatite. Geochimica et Cosmochimica Acta 69, 1847-1859.

Belousova, E. A., Griffin, W. L., O'Reilly, S. Y., and Fisher, N. I., 2002. Apatite as an indicator mineral for mineral exploration: trace-element compositions and their relationship to host rock type. Journal of Geochemical Exploration 76, 45-69.

Bickford, M. E., Cullers, R. L., Shuster, R. D., Premo, W. R., Van Schmus, W. R., Grambling, J. A., and Tewksbury, B. J., 1989. U-Pb zircon geochronology of Proterozoic and Cambrian plutons in the Wet Mountains and southern Front Range, Colorado, Proterozoic Geology of the Southern Rocky Mountains. Geological Society of America.

Bingen, B., Demaiffe, D., and Hertogen, J., 1996. Redistribution of rare earth elements, thorium, and uranium over accessory minerals in the course of amphibolite to granulite facies metamorphism: The role of apatite and monazite in orthogneisses from southwestern Norway. Geochimica et Cosmochimica Acta 60, 1341-1354.

Black, L. P., Kamo, S. L., Allen, C. M., Davis, D. W., Aleinikoff, J. N., Valley, J. W., Mundil, R., Campbell, I. H., Korsch, R. J., Williams, I. S., and Foudoulis, C., 2004. Improved 206Pb/238U microprobe geochronology by the monitoring of a trace-element-related matrix effect; SHRIMP, ID–TIMS, ELA–ICP–MS and oxygen isotope documentation for a series of zircon standards. Chemical Geology 205, 115-140.

Bros, R., Carpena, J., Sere, V., and Beltritti, A., 1996. Occurrence of Pu and fissiogenic REE in hydrothermal apatites from the fossil nuclear reactor 16 at Oklo (Gabon). Radiochimica Acta 74, 277-282.

Bruand, E., Fowler, M., Storey, C., Laurent, O., Antoine, C., Guitreau, M., Heilimo, E., and Nebel, O., 2020. Accessory mineral constraints on crustal evolution: elemental fingerprints for magma discrimination. Geochemical Perspectives Letters 13, 7-12.

Cao, M., Li, G., Qin, K., Seitmuratova, E. Y., and Liu, Y., 2012. Major and Trace Element Characteristics of Apatites in Granitoids from Central Kazakhstan: Implications for Petrogenesis and Mineralization. Resource Geology 62, 63-83.

Carr, P. A., Zink, S., Bennett, V. C., Norman, M. D., Amelin, Y., and Blevin, P. L., 2020. A new method for U-Pb geochronology of cassiterite by ID-TIMS applied to the Mole Granite polymetallic system, eastern Australia. Chemical Geology 539.

Chamberlain, K. R. and Bowring, S. A., 2001. Apatite–feldspar U–Pb thermochronometer: a reliable, mid-range (~450°C), diffusion-controlled system. Chemical Geology 172, 173-200.

Cherniak, D. J., Lanford, W. A., and Ryerson, F. J., 1991. Lead diffusion in apatite and zircon using ion implantation and Rutherford Backscattering techniques. Geochimica et Cosmochimica Acta 55, 1663-1673.

Chew, D., Drost, K., and Petrus, J. A., 2019. Ultrafast, > 50 Hz LA-ICP-MS Spot Analysis Applied to U–Pb Dating of Zircon and other U-Bearing Minerals. Geostandards and Geoanalytical Research 43, 39-60.

Chew, D. M., Babechuk, M. G., Cogné, N., Mark, C., O'Sullivan, G. J., Henrichs, I. A., Doepke, D., and McKenna, C. A., 2016. (LA,Q)-ICPMS trace element analyses of Durango and McClure Mountain apatite and implications for making natural LA-ICPMS mineral standards. Chemical Geology 435, 35-48.

Chew, D. M., Petrus, J. A., and Kamber, B. S., 2014. U–Pb LA–ICPMS dating using accessory mineral standards with variable common Pb. Chemical Geology 363, 185-199.

Chew, D. M. and Spikings, R. A., 2015. Geochronology and Thermochronology Using Apatite: Time and Temperature, Lower Crust to Surface. Elements 11, 189-194.

Chew, D. M., Sylvester, P. J., and Tubrett, M. N., 2011. U–Pb and Th–Pb dating of apatite by LA-ICPMS. Chemical Geology 280, 200-216.

Chiarenzelli, J. R., Lupulescu, M. V., Regan, S. P., and Singer, J. W., 2018. Age and Origin of the Mesoproterozoic Iron Oxide-Apatite Mineralization, Cheever Mine, Eastern Adirondacks, NY. Geosciences 8, 345.

Chiarenzelli, J. R. and McLelland, J. M., 1991. Age and Regional Relationships of Granitoid Rocks of the Adirondack Highlands. The Journal of Geology 99, 571-590.

Davis, W. J., Pestaj, T., Rayner, N., and McNicoll, V. M., 2018. Long-term reproducibility of 207Pb/206Pb age at the GSC SHRIMP lab based on the GSC Archean reference zircon z1242. 9th Inter. SHRIMP work., Korea Basic Science Institute, 107 p.

Farley, K. A., 2000. Helium diffusion from apatite: General behavior as illustrated by Durango fluorapatite. Journal of Geophysical Research: Solid Earth 105, 2903-2914.

Finger, F., Broska, I., Roberts, M. P., and Schermaier, A., 1998. Replacement of primary monazite by apatite-allanite-epidote coronas in an amphibolite facies granite gneiss from the Eastern Alps. American Mineralogist 83, 248-258.

Ghazi, M. J., Harris, C., Rahgoshay, M., and Moazzen, M., 2019. Combined igneous and hydrothermal source for the Kiruna-type Bafq magnetite-apatite deposit in Central Iran; trace element and oxygen isotope studies of magnetite. Ore Geology Reviews 105, 590-604.

Green, P. F., Duddy, I. R., Gleadow, A. J. W., Tingate, P. R., and Laslett, G. M., 1986. Thermal annealing of fission tracks in apatite: 1. A qualitative description. Chemical Geology: Isotope Geoscience section 59, 237-253.

Hagner, A. F. and Collins, L. G., 1967. Magnetite ore formed during regional metamorphism, Ausable magnetite district, New York. Economic Geology 62, 1034-1071.

Harlov, D. E., 2015. Apatite: A Fingerprint for Metasomatic Processes. Elements 11, 171-176.

Harlov, D. E., Andersson, U. B., Förster, H.-J., Nyström, J. O., Dulski, P., and Broman, C., 2002. Apatite–monazite relations in the Kiirunavaara magnetite–apatite ore, northern Sweden. Chemical Geology 191, 47-72.

Harlov, D. E., Meighan, C. J., Kerr, I. D., and Samson, I. M., 2016. Mineralogy, Chemistry, and Fluid-Aided Evolution of the Pea Ridge Fe Oxide-(Y + REE) Deposit, Southeast Missouri, USA. Economic Geology 111, 1963-1984.

Harlov, D. E., Wirth, R., and Förster, H.-J., 2005. An experimental study of dissolution–reprecipitation in fluorapatite: fluid infiltration and the formation of monazite. Contributions to Mineralogy and Petrology 150, 268-286.

Heinrich, E. W. and Dahlem, D. H., 1969. Dikes of the McClure mountain — Iron mountain alkalic complex, Fremont county, Colorado, U.S.A. Bulletin Volcanologique 33, 960-976.

Hiess, J., Condon, D. J., McLean, N., and Noble, S. R., 2012. 238U/235U systematics in terrestrial uranium-bearing minerals. Science 335, 1610-1614.

Hu, Z., Gao, S., Liu, Y., Hu, S., Chen, H., and Yuan, H., 2008. Signal enhancement in laser ablation ICP-MS by addition of nitrogen in the central channel gas. Journal of Analytical Atomic Spectrometry 23, 1093-1101.

Huyskens, M. H., Iizuka, T., and Amelin, Y., 2012. Evaluation of colloidal silicagels for lead isotopic measurements using thermal ionisation mass spectrometry. Journal of Analytical Atomic Spectrometry 27, 1439-1446.

Jaffey, A. H., Flynn, K. F., Glendenin, L. E., Bentley, W. C., and Essling, A. M., 1971. Precision Measurement of Half-Lives and Specific Activities of 235U and 238U. Physical Review C 4, 1889-1906.

Jochum, K. P. and Stoll, B., 2008. Reference materials for elemental and isotopic analyses by LA-(MC)-ICP-MS: Successes and outstanding needs. In: Sylvester, P. (Ed.), Laser Ablation ICP-MS in the Earth Sciences: Current practices and outstanding issues (pp. 147-168). Mineralogical Association of Canada, Quebec.

Kirkland, C. L., Yakymchuk, C., Szilas, K., Evans, N., Hollis, J., McDonald, B., and Gardiner, N. J., 2018. Apatite: a U-Pb thermochronometer or geochronometer? Lithos 318-319, 143-157.

Klein, T., Evans, K., and DeWitt, E., 2010. Geochronology database for central Colorado. US Geol Surv Data Ser 2009, 489.

Knipping, J. L., Bilenker, L. D., Simon, A. C., Reich, M., Barra, F., Deditius, A. P., Wälle, M., Heinrich, C. A., Holtz, F., and Munizaga, R., 2015. Trace elements in magnetite from massive iron oxide-apatite deposits indicate a combined formation by igneous and magmatic-hydrothermal processes. Geochimica et Cosmochimica Acta 171, 15-38.

Krogstad, E. J. and Walker, R. J., 1994. High closure temperatures of the U-Pb system in large apatites from the Tin Mountain pegmatite, Black Hills, South Dakota, USA. Geochimica et Cosmochimica Acta 58, 3845-3853.

Laslett, G. M., Green, P. F., Duddy, I. R., and Gleadow, A. J. W., 1987. Thermal annealing of fission tracks in apatite 2. A quantitative analysis. Chemical Geology: Isotope Geoscience section 65, 1-13.

Ludwig, K., 2009. Squid 2, version 2.50, A user's manual. Berkeley Geochronology Center, Special Publication, 110.

Ludwig, K., 2012. User's manual for Isoplot 3.75. A geological toolkit for Microsoft Excel, Berkeley Geochronology Center Special Publication No. 5.

Ludwig, K. R., 1998. On the treatment of concordant uranium-lead ages. Geochimica et Cosmochimica Acta 62, 665-676.

Lupulescu, M., Chiarenzelli, J., Selleck, B., McLelland, J., and Regan, S., 2016. LA-MC-ICPMS U/Pb zircon geochronology of the Grenville age iron deposits of New York, Geological Society of America Abstracts with Programs.

Lupulescu, M. V., Chiarenzelli, J. R., Pullen, A. T., and Price, J. D., 2011. Using pegmatite geochronology to constrain temporal events in the Adirondack Mountains. Geosphere 7, 23-39.

Lupulescu, M. V., Hughes, J. M., Chiarenzelli, J. R., and Bailey, D. G., 2017. Texture, Crystal Structure, and Composition of Fluorapatites from Iron Oxide-apatite (ioa) Deposits, Eastern Adirondack Mountains, New York. The Canadian Mineralogist 55, 399-417.

Mank, J. G. A. and Mason, R. D. P., 1999. A critical assessment of laser ablation ICP-MS as an analytical tool for depth analysis in silica-based glass samples. Journal of Analytical Atomic Spectrometry 14, 1143-1153.

Mao, M., Rukhlov, A. S., Rowins, S. M., Spence, J., and Coogan, L. A., 2016. Apatite Trace Element Compositions: A Robust New Tool for Mineral Exploration. Economic Geology 111, 1187-1222.

McDowell, F. W., McIntosh, W. C., and Farley, K. A., 2005. A precise 40Ar–39Ar reference age for the Durango apatite (U–Th)/He and fission-track dating standard. Chemical Geology 214, 249-263.

McLelland, J., Hamilton, M., Selleck, B., McLelland, J., Walker, D., and Orrell, S., 2001. Zircon U-Pb geochronology of the Ottawan Orogeny, Adirondack Highlands, New York: regional and tectonic implications. Precambrian Research 109, 39-72.

Mclelland, J., Morrison, J., Selleck, B., Cunningham, B., Olson, C., and Schmidt, K., 2002. Hydrothermal alteration of late- to post-tectonic Lyon Mountain Granitic Gneiss, Adirondack Mountains, New York: Origin of quartz–sillimanite segregations, quartz–albite lithologies, and associated Kiruna-type low-Ti Fe-oxide deposits. Journal of Metamorphic Geology 20, 175-190.

McLelland, J. M. and Selleck, B. W., 2011. Megacrystic Gore Mountain–type garnets in the Adirondack Highlands: Age, origin, and tectonic implications. Geosphere 7, 1194-1208.

McLelland, J. M., Selleck, B. W., and Bickford, M. E., 2013. Tectonic Evolution of the Adirondack Mountains and Grenville Orogen Inliers within the USA. Geoscience Canada 40, 318–352.

Mercer, C. N., Watts, K. E., and Gross, J., 2020. Apatite trace element geochemistry and cathodoluminescent textures - a comparison between regional magmatism and the Pea Ridge IOAREE and Boss IOCG deposits, southeastern Missouri iron metallogenic province, USA. Ore Geology Reviews 116, 103-129.

Miller, A. R., Cumming, G. L., and Krstic, D., 1989. U–Pb, Pb–Pb, and K–Ar isotopic study and petrography of uraniferous phosphate-bearing rocks in the Thelon Formation,

Dubawnt Group, Northwest Territories, Canada. Canadian Journal of Earth Sciences 26, 867-880.

Neymark, L., Hall, S., and Breit, G., 2019. High Spatial Resolution in situ LA-ICPMS U-Pb Geochronology of Titanite and Apatite from the Coles Hill Uranium Deposit, Virginia, USA. Goldschmidt Conference, Barcelona.

Neymark, L., Holm-Denoma, C. S., Pietruszka, A., Aleinikoff, J. N., Fanning, C. M., Pillers, R. M., and Moscati, R. J., 2016. High spatial resolution U-Pb geochronology and Pb isotope geochemistry of magnetite-apatite ore from the Pea Ridge iron oxide-apatite deposit, St. Francois Mountains, southeast Missouri, USA. Economic Geology 111, 1915-1933.

O'Sullivan, G., Chew, D., Kenny, G., Henrichs, I., and Mulligan, D., 2020. The trace element composition of apatite and its application to detrital provenance studies. Earth-Science Reviews 201.

O'Sullivan, G. J. and Chew, D. M., 2020. The clastic record of a Wilson Cycle: Evidence from detrital apatite petrochronology of the Grampian-Taconic fore-arc. Earth and Planetary Science Letters 552, 116588.

Olson, J. C., Marvin, R. F., Parker, R. L., and Mehnert, H. H., 1977. Age and tectonic setting of lower Paleozoic alkalic and mafic rocks, carbonatites, and thorium veins in south-central Colorado. US Geological Survey Journal of Research 5, 673-687.

Palma, G., Barra, F., Reich, M., Valencia, V., Simon, A. C., Vervoort, J., Leisen, M., and Romero, R., 2019. Halogens, trace element concentrations, and Sr-Nd isotopes in apatite from iron oxide-apatite (IOA) deposits in the Chilean iron belt: Evidence for magmatic and hydrothermal stages of mineralization. Geochimica et Cosmochimica Acta 246, 515-540.

Pan, L.-C., Hu, R.-Z., Wang, X.-S., Bi, X. W., Zhu, J.-J., and Li, C., 2016. Apatite trace element and halogen compositions as petrogenetic-metallogenic indicators: Examples from four granite plutons in the Sanjiang region, SW China. Lithos 254-255, 118-130.

Pan, Y. and Fleet, M. E., 2002. Compositions of the Apatite-Group Minerals: Substitution Mechanisms and Controlling Factors. Reviews in Mineralogy and Geochemistry 48, 13-49.

Parrish, R. R., 1990. U–Pb dating of monazite and its application to geological problems. Canadian Journal of Earth Sciences 27, 1431-1450.

Paton, C., Hellstrom, J., Paul, B., Woodhead, J., and Hergt, J., 2011. Iolite: Freeware for the visualisation and processing of mass spectrometric data. Journal of Analytical Atomic Spectrometry 26, 2508-2518.

Pietruszka, A. J. and Neymark, L. A., 2017. Evaluation of laser ablation double-focusing SC-ICPMS for "common" lead isotopic measurements in silicate glasses and minerals. Journal of Analytical Atomic Spectrometry 32, 1135-1154.

Pivarunas, A. F. and Meert, J. G., 2019. Protracted magmatism and magnetization around the McClure Mountain alkaline igneous complex. Lithosphere 11, 590-602.

Postel, A. W., 1952. Geology of the Clinton County magnetite district, New York. U.S. Geol. Surv. Pro. Paper 237, 88 p.

Regan, S., Lupulescu, M., Jercinovic, M., Chiarenzelli, J., Williams, M., Singer, J., and Bailey, D., 2019. Age and Origin of Monazite Symplectite in an Iron Oxide-Apatite Deposit in the Adirondack Mountains, New York, USA: Implications for Tracking Fluid Conditions. Minerals 9, 65.

Renne, P. R., Swisher, C. C., Deino, A. L., Karner, D. B., Owens, T. L., and DePaolo, D. J., 1998. Intercalibration of standards, absolute ages and uncertainties in 40Ar/39Ar dating. Chemical Geology 145, 117-152.

Rivers, T., 2015. Tectonic Setting and Evolution of the Grenville Orogen: An Assessment of Progress Over the Last 40 Years. Geoscience Canada 42, 77-124.

Romer, R. L., 1996. U-Pb systematics of stilbite-bearing low-temperature mineral assemblages from the Malmberget iron ore, northern Sweden. Geochimica et Cosmochimica Acta 60, 1951-1961.

Romer, R. L. and Rötzler, J., 2003. Effect of metamorphic reaction history on the U-Pb dating of titanite. Geological Society, London, Special Publications 220, 147-158.

Samson, S. D. and Alexander, E. C., 1987. Calibration of the interlaboratory 40Ar-39Ar dating standard, MMhb-1. Chemical Geology: Isotope Geoscience section 66, 27-34.

Schärer, U., 1984. The effect of initial 230Th disequilibrium on young UPb ages: the Makalu case, Himalaya. Earth and Planetary Science Letters 67, 191-204.

Schmitz, M. D. and Schoene, B., 2007. Derivation of isotope ratios, errors, and error correlations for U-Pb geochronology using 205Pb-235U-(233U)-spiked isotope dilution thermal ionization mass spectrometric data. Geochemistry, Geophysics, Geosystems 8.

Schoene, B. and Bowring, S. A., 2006. U–Pb systematics of the McClure Mountain syenite: thermochronological constraints on the age of the 40Ar/39Ar standard MMhb. Contributions to Mineralogy and Petrology 151, 615.

Shaw, R. A., Goodenough, K. M., Roberts, N. M. W., Horstwood, M. S. A., Chenery, S. R., and Gunn, A. G., 2016. Petrogenesis of rare-metal pegmatites in high-grade metamorphic terranes: A case study from the Lewisian Gneiss Complex of north-west Scotland. Precambrian Research 281, 338-362.

Shawe, D. R. and Parker, R. L., 1967. Mafic-ultramafic layered intrusion at Iron Mountain, Fremont County, ColoradoBulletin.

Simon, A. C., Knipping, J., Reich, M., Barra, F., Deditius, A. P., Bilenker, L., and Childress, T., 2018. Kiruna-Type Iron Oxide-Apatite (IOA) and Iron Oxide Copper-Gold (IOCG) Deposits Form by a Combination of Igneous and Magmatic-Hydrothermal Processes: Evidence from the Chilean Iron Belt. In: Arribas R, A. M. and Mauk, J. L. (editors), Metals, Minerals, and Society. Society of Economic Geologists (SEG).

Smith, S. R., Foster, G. L., Romer, R. L., Tindle, A. G., Kelley, S. P., Noble, S. R., Horstwood, M., and Breaks, F. W., 2004. U-Pb columbite-tantalite chronology of rare-element pegmatites using TIMS and Laser Ablation-Multi Collector-ICP-MS. Contributions to Mineralogy and Petrology 147, 549-564.

Smye, A. J., Marsh, J. H., Vermeesch, P., Garber, J. M., and Stockli, D. F., 2018. Applications and limitations of U-Pb thermochronology to middle and lower crustal thermal histories. Chemical Geology 494, 1-18.

Souders, A. K. and Sylvester, P. J., 2010. Accuracy and precision of non-matrix-matched calibration for lead isotope ratio measurements of lead-poor minerals by LA-MC-ICPMS. Journal of Analytical Atomic Spectrometry 25, 975-988.

Spell, T. L. and McDougall, I., 2003. Characterization and calibration of 40Ar/39Ar dating standards. Chemical Geology 198, 189-211.

Stacey, J. S. and Kramers, J. D., 1975. Approximation of terrestrial lead isotope evolution by a two-stage model. Earth and Planetary Science Letters 26, 207-221.

Su, Z.-K., Zhao, X.-F., Zeng, L.-P., Zhao, K.-D., and Hofstra, A. H., 2019. Tourmaline boron and strontium isotope systematics reveal magmatic fluid pulses and external fluid influx in a giant iron oxide-apatite (IOA) deposit. Geochimica et Cosmochimica Acta 259, 233-252.

Sylvester, P. J. and Jackson, S. E., 2016. A Brief History of Laser Ablation Inductively Coupled Plasma Mass Spectrometry (LA–ICP–MS). Elements 12, 307-310.

Taylor, R. D., Shah, A. K., Walsh, G. J., and Taylor, C. D., 2019. Geochemistry and Geophysics of Iron Oxide-Apatite Deposits and Associated Waste Piles with Implications for Potential Rare Earth Element Resources from Ore and Historical Mine Waste in the Eastern Adirondack Highlands, New York, USA. Economic Geology 114, 1569-1598.

Tera, F. and Wasserburg, G. J., 1972. U-Th-Pb systematics in three Apollo 14 basalts and the problem of initial Pb in lunar rocks. Earth and Planetary Science Letters 14, 281-304.

Thomson, S. N., Gehrels, G. E., Ruiz, J., and Buchwaldt, R., 2012. Routine low-damage apatite U-Pb dating using laser ablation–multicollector–ICPMS. Geochemistry, Geophysics, Geosystems 13.

Valley, P. M., Hanchar, J. M., and Whitehouse, M. J., 2009. Direct dating of Fe oxide-(Cu-Au) mineralization by U/Pb zircon geochronology. Geology, 37, 223-226.

Valley, P. M., Hanchar, J. M., and Whitehouse, M. J., 2011. New insights on the evolution of the Lyon Mountain Granite and associated Kiruna-type magnetite-apatite deposits, Adirondack Mountains, New York State. Geosphere 7, 357-389.

van Soest, M. C., Monteleone, B. D., Hodges, K. V., and Boyce, J. W., 2011. Laser depth profiling studies of helium diffusion in Durango fluorapatite. Geochimica et Cosmochimica Acta 75, 2409-2419.

Vanhaecke, F., 2012. Single-collector inductively coupled plasma mass spectrometry. In: Vanhaecke, F. and Degryse, P. (editors), Isotopic analysis: Fundamentals and applications using ICP-MS. Wiley-VCH.

Veríssimo, C. U. V., Santos, R. V., Parente, C. V., Oliveira, C. G. d., Cavalcanti, J. A. D., and Nogueira Neto, J. d. A., 2016. The Itataia phosphate-uranium deposit (Ceará, Brazil) new petrographic, geochemistry and isotope studies. Journal of South American Earth Sciences 70, 115-144.

Wang, T., Tong, Y., Jahn, B.-m., Zou, T.-r., Wang, Y.-b., Hong, D.-w., and Han, B.-f., 2007. SHRIMP U–Pb Zircon geochronology of the Altai No. 3 Pegmatite, NW China, and its implications for the origin and tectonic setting of the pegmatite. Ore Geology Reviews 32, 325-336.

Wetherill, G. W., 1956. Discordant uranium-lead ages, I. Eos, Transactions American Geophysical Union 37, 320-326.

Whitney, P. R. and Olmsted, J. F., 1993. Bedrock geology of the Au Sable Forks quadrangle, northeastern Adirondack Mountains, New York. New York State Museum Map and Chart Series No. 43, 48 p.

Whittaker, E. J. W. and Muntus, R., 1970. Ionic radii for use in geochemistry. Geochimica et Cosmochimica Acta 34, 945-956.

Williams, I. S., 1998. U-Th-Pb geochronology by ion microprobe. Reviews in economic geology 7, 1-35.

Yang, Y.-H., Wu, F.-Y., Yang, J.-H., Chew, D. M., Xie, L.-W., Chu, Z.-Y., Zhang, Y.-B., and Huang, C., 2014. Sr and Nd isotopic compositions of apatite reference materials used in U–Th–Pb geochronology. Chemical Geology 385, 35-55.

Yu, Z.-Q., Ling, H.-F., Mavrogenes, J., Chen, P.-R., Chen, W.-F., and Fang, Q.-C., 2019. Metallogeny of the Zoujiashan uranium deposit in the Mesozoic Xiangshan volcanic-intrusive complex, southeast China: Insights from chemical compositions of hydrothermal apatite and metal elements of individual fluid inclusions. Ore Geology Reviews 113, 103085.

Zhang, L.-S. and Schärer, U., 1996. Inherited Pb components in magmatic titanite and their consequence for the interpretation of U-Pb ages. Earth and Planetary Science Letters 138, 57-65.

Table 1. Apatite standards used most frequently for in situ dating

Apatite standard	Age, Ma	Pb, ppm	U, ppm	Comments
Durango	31.44 ± 0.18	0.5-3	Up to 12-13, variable	^{40}Ar-^{39}Ar age. Used as a standard for f track and (U-Th)/He da
McClure Mountain (MMap)	523.51 ± 1.47	3-4	16-18	ID-TIMS, total Pb/U iso age
Madagascar (MAD)	486.58 ± 0.85 (MAD1) and 47[illegible] ± 0.41 (MAD2)	26	23	^{206}Pb/^{238}U ID-TIMS ag
Kovdor	376.4 ± 0.[illegible]	0.7-4	0.2-3.6	ID-TIMS Th-Pb age. Th content of 62-150 p

Journal Pre-proof

Table 2. ID-TIMS U-Pb isotopic data for apatite

		Compositional Parameters					Radiogenic Isotope Ratios									
Location	Sample	U ppm	Th/U	Pb ppm	Pb*/Pbc	Pbc pg	$^{206}Pb/^{204}Pb$	$^{208}Pb/^{204}Pb$	$^{208}Pb/^{206}Pb$	$^{207}Pb/^{206}Pb$	%err	$^{207}Pb/^{235}U$	%err	$^{206}Pb/^{238}U$	%err	corr. coef.
	(a)	(b)	(c)	(b)	(d)	(d)	(e)	(e)	(f)	(f)	(g)	(f)	(g)	(f)	(g)	
Cheever mine	A148 01	274.7	3.2	79.2	113	15.6	3916	3831	0.97	0.071765	0.04	1.6010	0.08	0.16187	0.07	0.85
	A148 02	132.1	4.6	49.2	93	18.8	2650	3740	1.41	0.073814	0.12	1.7502	0.20	0.17205	0.15	0.79
	A148 03	156.8	6.0	66.6	134	15.1	3251	5962	1.83	0.072924	0.05	1.6878	0.07	0.16793	0.04	0.69
	A148 04	130.3	4.6	47.9	83	13.8	2365	3326	1.40	0.073222	0.05	1.7140	0.06	0.16985	0.04	0.58
	A148 05	142.5	5.1	55.5	105	66.8	2819	4379	1.55	0.073409	0.04	1.7205	0.07	0.17006	0.06	0.81
	A148 06	183.9	4.4	63.6	146	24.9	4264	5752	1.35	0.072246	0.03	1.6365	0.06	0.16435	0.05	0.88
	A148 07	172.0	4.0	57.2	123	21.0	3779	4674	1.23	0.072515	0.03	1.6543	0.10	0.16553	0.09	0.95
	A148 08	172.2	4.0	57.0	130	25.7	3981	4909	1.23	0.072457	0.03	1.6509	0.06	0.16533	0.05	0.88
	A148 09	176.9	4.6	63.0	135	7.9	3814	5422	1.42	0.072318	0.04	1.6384	0.08	0.16439	0.07	0.86
	A148 10	185.4	4.4	63.7	139	4.1	4046	5426	1.34	0.072163	0.06	1.6289	0.09	0.16379	0.07	0.76
	A148 11	170.2	5.2	65.4	91	6.0	2416	3843	1.59	0.072442	0.08	1.6504	0.10	0.16531	0.06	0.61
	A148 12	92.9	5.3	36.6	111	2.0	2919	4690	1.60	0.073033	0.15	1.7004	0.17	0.16894	0.08	0.51
	A148 13	168.8	5.2	65.0	128	3.1	3386	5372	1.58	0.072725	0.08	1.6686	0.13	0.16648	0.10	0.77
	A148 14	141.8	6.0	61.4	120	8.1	2916	5359	1.84	0.073412	0.06	1.7269	0.09	0.17068	0.07	0.77
Old Bed mine	A154 01	177.5	5.3	68.9	78	67.0	2164	3487	1.61	0.072406	0.05	1.6515	0.09	0.16550	0.07	0.81
	A154 02	139.7	5.7	60.6	49	57.4	1295	2261	1.74	0.074047	0.08	1.7813	0.09	0.17455	0.06	0.57
	A154 03	238.5	3.2	68.6	77	51.3	2779	2749	0.99	0.071361	0.04	1.5747	0.06	0.16011	0.05	0.81
	A154 05	151.3	6.9	69.6	93	35.8	2181	4571	2.10	0.072458	0.05	1.6580	0.28	0.16604	0.28	0.98
	A154 07	145.6	5.0	56.7	57	66.0	1624	2501	1.53	0.073165	0.06	1.7126	0.08	0.16984	0.04	0.57
	A154 09	282.0	4.6	99.2	106	53.3	3176	4456	1.40	0.071951	0.03	1.6189	0.09	0.16326	0.08	0.93
	A154 10	141.7	5.1	54.7	50	61.4	1434	2213	1.54	0.072728	0.08	1.6792	0.10	0.16753	0.07	0.70
	A156 01	152.8	4.1	54.6	43	30.9	1357	1744	1.26	0.073848	0.08	1.7669	0.10	0.17361	0.06	0.62
	A156 02	341.7	6.6	152.7	102	38.1	2467	4954	2.01	0.072467	0.04	1.6589	0.07	0.16611	0.06	0.79
	A156 03	169.0	4.1	55.3	114	21.7	3655	4597	1.25	0.071604	0.04	1.5930	0.07	0.16143	0.06	0.83
	A156 05	214.0	3.8	69.4	65	13.5	2175	2569	1.17	0.072123	0.05	1.6374	0.08	0.16473	0.06	0.75
	A156 06	142.6	3.7	46.0	56	32.1	1898	2186	1.14	0.072336	0.06	1.6512	0.09	0.16563	0.07	0.78
	A156 07	172.5	4.7	63.9	49	1.8	1449	2103	1.44	0.072650	0.08	1.6724	0.10	0.16703	0.06	0.58
	A156 08	133.2	5.4	55.6	47	33.6	1309	2152	1.64	0.073975	0.09	1.7787	0.11	0.17447	0.05	0.52
McClure Mountains	A149 01	10.6	5.4	3.5	1.5	89.6	58	104	1.66	0.056604	3.55	0.6475	3.69	0.08300	0.77	0.28
	A149 03	10.8	4.8	3.0	2.1	56.8	78	127	1.49	0.057708	2.02	0.6680	2.07	0.08399	0.51	0.23
	A149 04	10.2	5.0	3.0	1.9	53.9	71	120	1.56	0.058081	2.30	0.6706	2.37	0.08378	0.57	0.24
	A149 05	11.7	4.3	3.1	1.9	53.6	76	116	1.34	0.057143	2.12	0.6611	2.18	0.08395	0.52	0.23
	A151 01	9.4	4.8	2.7	1.9	18.8	73	120	1.50	0.057737	2.21	0.6601	2.27	0.08295	0.55	0.24
	A151 02	7.1	5.5	2.7	1.1	24.0	48	88	1.69	0.056429	4.13	0.6442	4.24	0.08283	1.02	0.23
	A151 03	23.3	3.6	5.0	2.7	22.6	111	142	1.12	0.057416	1.31	0.6631	1.35	0.08380	0.33	0.24
	A151 04	8.1	4.9	2.4	1.7	18.6	67	113	1.54	0.057436	2.54	0.6591	2.62	0.08326	0.62	0.24
	A151 05	12.6	5.1	3.1	4.2	12.1	131	227	1.68	0.057815	1.09	0.6709	1.12	0.08421	0.27	0.25
	A151 06	23.3	5.4	5.6	4.7	18.8	147	252	1.67	0.057431	0.95	0.6666	0.98	0.08421	0.24	0.25
	A151 07	12.0	5.2	3.1	3.0	14.6	101	172	1.63	0.058159	1.45	0.6747	1.50	0.08417	0.38	0.25
	A151 08	21.7	5.0	3.9	4.0	13.8	167	179	0.95	0.057757	0.84	0.6707	0.87	0.08426	0.21	0.27
	A151 09	5.8	5.1	1.8	1.6	14.5	63	110	1.60	0.057670	2.75	0.6595	2.84	0.08298	0.67	0.25
	A151 10	18.3	8.4	6.9	2.3	41.1	64	157	2.60	0.056768	2.66	0.6471	2.74	0.08272	0.66	0.23
	A151 11	13.2	5.9	3.8	2.6	21.3	85	160	1.85	0.057374	1.84	0.6602	1.89	0.08349	0.45	0.24
	A151 12	5.4	4.4	1.9	1.0	17.8	49	79	1.34	0.056141	4.12	0.6376	4.24	0.08241	1.00	0.24
	A151 13	17.1	5.2	4.5	2.9	19.1	99	171	1.63	0.057847	1.48	0.6686	1.52	0.08386	0.37	0.24
	A151 14	8.6	6.7	3.2	1.6	24.1	56	115	2.07	0.056605	3.27	0.6446	3.36	0.08263	0.81	0.23

(a) Labels for apatite fractions.
(b) Nominal U and total Pb concentrations.
(c) Model Th/U ratio calculated from radiogenic $^{208}Pb/^{206}Pb$ ratio and $^{207}Pb/^{235}U$ age.
(d) Pb* and Pbc represent radiogenic and initial (common) Pb, respectively.
(e) Measured ratio corrected for spike and fractionation only.
(f) Corrected for fractionation, spike, and common Pb.

(g) Errors are 2-sigma, propagated using the algorithms of (SCHMITZ AND SCHOENE, 2007).

(h) Calculations are based on the decay constants of (JAFFEY et al., 1971) and a $^{238}U/^{235}U$ ratio of 137.818 (HIESS et al., 2012). $^{206}Pb/^{238}U$ and $^{207}Pb/^{206}Pb$ ages corrected for initial disequilibrium in $^{230}Th/^{238}U$ using Th/U [magma] = 3.

Journal Pre-proof

Journal Pre-proof

Table 3. U-Th-Pb isotope data for Old Bed Mine zircon collected by SHRIMP II

Spot ID	U, ppm	Th, ppm	$^{204}Pb/^{206}Pb$	± 1σ %	$^{208}Pb/^{206}Pb$	± 1σ %	$^{238}U/^{206}Pb$	± 1σ %	$^{207}Pb/^{206}Pb$	± 1σ %	S-K_{cor} $^{207}Pb^*/^{206}Pb^*$	± 1σ %	S-K_{cor} $^{207}Pb^*/^{235}U$	± 1σ %	S-K_{cor} $^{206}Pb^*/^{238}U$[a]	± 1σ %	Rho[b]	$^{206}Pb^*/^{238}U$ Age, Ma[c]	± 2σ Ma
Cores																			
11512-001.1	448	61	-2.2 E-5	50	0.042	3.83	5.86	0.91	0.0735	0.55	0.0738	0.58	1.74	1.11	0.1708	0.91	0.84	1017	19
11512-002.1	580	84	1.3 E-5	58	0.045	2.23	5.93	0.84	0.0732	0.49	0.0730	0.51	1.70	1.01	0.1687	0.84	0.85	1005	17
11512-003.1	540	76	5.8 E-5	29	0.043	2.53	6.08	0.98	0.0736	0.51	0.0728	0.6	1.6	1.21	0.1642	0.98	0.85	980	19
11512-005.1	474	65	---	---	0.046	2.53	5.91	0.91	0.0731	0.54	0.0731	0.54	1.70	1.11	0.1691	0.91	0.86	1007	18
11512-004.1	454	55	2.2 E-5	50	0.038	2.94	5.93	1.02	0.0736	0.55	0.0733	0.59	1.70	1.21	0.1686	1.02	0.87	1004	21
11512-006.1	438	53	1.8 E-5	58	0.038	2.03	5.96	0.85	0.0733	0.56	0.0730	0.60	1.69	1.01	0.1678	0.85	0.82	1000	17
11512-006.2	527	76	3.9 E-5	35	0.046	2.44	5.90	0.84	0.0735	0.51	0.0730	0.58	1.70	1.01	0.1694	0.84	0.82	1009	17
11512-007.1	429	50	1.8 E-5	58	0.037	2.23	5.91	0.85	0.0719	0.60	0.0717	0.63	1.67	1.11	0.1690	0.85	0.80	1007	17
11512-008.1	400	49	3.6 E-5	41	0.043	2.83	5.85	0.85	0.0733	0.57	0.0727	0.65	1.71	1.11	0.1710	0.85	0.80	1017	17
11512-009.1	613	89	2.1 E-5	45	0.045	2.33	5.94	0.83	0.0725	0.48	0.0722	0.52	1.68	1.01	0.1683	0.83	0.85	1003	17
11512-011.1	487	68	1.0 E-5	71	0.044	2.53	5.88	0.84	0.0731	0.53	0.0729	0.55	1.71	1.01	0.1700	0.84	0.84	1012	17
11512-012.1	497	51	4.8 E-6	10	0.036	2.74	5.91	0.84	0.0723	0.51	0.0722	0.52	1.69	1.01	0.1693	0.84	0.85	1008	17
11512-013.1	410	48	---	00	0.042	3.06	5.97	0.85	0.0730	0.58	0.0730	0.58	1.68	1.01	0.1674	0.85	0.82	998	17
11512-015.1	546	70	9.4 E-6	71	0.040	2.25	5.85	0.85	0.0733	0.50	0.0731	0.52	1.72	1.01	0.1708	0.85	0.85	1016	17
11512-017.1	466	79	1.1 E-5	71	0.055	2.43	5.88	0.84	0.0738	1.05	0.0736	1.06	1.73	1.41	0.1702	0.84	0.62	1013	17
11512-018.1	467	55	2.1 E-5	501	0.037	2.93	5.89	0.84	0.0729	0.53	0.0726	0.57	1.70	1.01	0.1698	0.84	0.83	1011	17
11512-019.1	560	78	4.3 E-6	00	0.044	2.4	5.88	0.83	0.0732	0.83	0.0731	0.83	1.71	1.2	0.1700	0.83	0.71	1012	17
Rims																			
11512-001.2	485	69	9.7 E-5	23	0.047	3.4	5.97	0.84	0.0742	0.52	0.0728	0.69	1.68	1.11	0.1671	0.84	0.77	996	17

Journal Pre-proof

11512-002.2	569	60	-4.5E-6	10	0.032	3.93	6.03	0.84	0.0724	0.49	0.0725	0.50	1.66	1.01	0.1659	0.84	0.86	989	17
11512-003.2	589	119	3.5E-5	35	0.046	2.22	6.05	1.06	0.0729	0.48	0.0724	0.55	1.65	2.11	0.1652	1.06	0.89	986	21
11512-004.2	604	244	1.2E-4	20	0.058	2.92	6.40	0.83	0.0736	0.49	0.0720	0.67	1.55	1.11	0.1560	0.84	0.78	935	16
11512-010.1	639	206	6.4E-5	25	0.056	2.72	6.13	0.88	0.0726	0.46	0.0717	0.57	1.61	0.11	0.1629	0.88	0.84	973	17
11512-012.2	608	171	1.5E-4	18	0.056	2.94	6.54	0.90	0.0729	0.49	0.0708	0.74	1.49	2.11	0.1525	0.90	0.77	915	17
11512-014.1	447	51	5.3E-6	00	0.035	0.07	5.93	0.84	0.0720	0.54	0.0720	0.55	1.67	0.11	0.1687	0.84	0.84	1005	17
11512-014.2	469	50	1.1E-5	71	0.033	0.03	5.97	0.84	0.0725	0.54	0.0723	0.57	1.66	0.11	0.1675	0.84	0.83	998	17
11512-016.1	614	102	2.3E-5	41	0.043	2.12	5.96	1.14	0.0720	0.46	0.0716	0.50	1.66	2.11	0.1676	1.14	0.92	999	23
11512-016.2	1351	122	2.8E-5	26	0.031	0.53	5.95	1.04	0.0706	0.32	0.0702	0.36	1.63	1.11	0.1680	1.04	0.95	1001	21
11512-020.1	633	85	1.2E-5	58	0.041	2.02	6.04	0.83	0.0722	0.46	0.0726	0.47	1.66	2.10	0.1656	0.83	0.87	988	16

[a]Isotope ratios corrected for initial Pb using 1Ga Stacey Kramers (S-K) model Pb composition ($^{206}Pb/^{204}Pb$ =17.068, $^{207}Pb/^{204}Pb$ = 15.510) and the measured abundance of ^{204}Pb.

[b]Rho - correlation coefficient between the initial-Pb-corrected $^{206}Pb^*/^{238}U$ and $^{207}Pb^*/^{235}U$ ratios.

[c]Age (Ma) calculated from the $^{206}Pb^*/^{238}U$ ratio corrected for the initial Pb using S-K model.

Journal Pre-proof

Table 4. U-Th-Pb isotope data for Old Bed Mine apatite collected using SHRIMP-RG

Spot ID	U, ppm	Th, ppm	$^{206}Pb/^{204}Pb$	± 1σ %	$^{208}Pb/^{206}Pb$	± 1σ %	Total $^{238}U/^{206}Pb$	± 1σ %	Total $^{207}Pb/^{206}Pb$	± 1σ %	S-K[a] $^{204}Pb_{corr}$ $^{238}U/^{206}Pb^*$	± 1σ %	S-K[a] $^{204}Pb_{corr}$ $^{207}Pb^*/^{206}Pb^*$	± 1σ %	S-K $^{204}Pb_{corr}$ $^{206}Pb^*/^{238}U$ Age, Ma[b]	± 1σ Ma
OBM-1-1.1	52.8	229	3145	5.0	1.21	1.9	5.95	3.2	0.076	1.4	5.98	3.2	0.0722	3.5	997	29
OBM-1-2.1	60.6	443	2090	3.8	1.81	1.5	5.80	4.0	0.079	1.4	5.90	4.0	0.0729	3.9	1009	37
OBM-1-3.1	60.2	305	2136	3.3	1.33	1.5	5.59	2.7	0.082	1.1	5.64	2.7	0.0735	3.2	1053	26
OBM-1-4.1	67.2	271	2463	3.8	1.07	1.8	5.98	2.6	0.080	2.2	6.02	2.6	0.0734	3.3	990	24
OBM-1-5.1	44.9	680	1030	2.8	3.61	1.1	5.21	2.8	0.083	1.3	5.29	2.8	0.0730	5.9	1115	29
OBM-1-6.1	85.7	420	3460	4.1	1.27	1.5	5.98	2.2	0.076	1.1	6.01	2.2	0.0726	2.6	991	20
OBM-1-7.1	61.3	468	1103	2.6	1.91	1.4	5.72	3.1	0.083	2.6	5.81	3.1	0.0730	5.8	1023	30
OBM-1-8.1	85.9	249	1485	2.8	0.78	1.9	6.19	2.0	0.079	1.1	6.26	2.0	0.0729	4.1	955	18
OBM-1-9.1	72.5	493	1725	3.0	1.75	2.5	5.67	3.1	0.079	1.1	5.72	3.1	0.0730	3.8	1038	30
OBM-1-10.1	59.3	260	1319	2.9	1.19	3.8	5.88	3.3	0.078	1.3	5.90	3.3	0.0729	5.0	1009	32
OBM-1-11.1	82.5	569	3404	4.1	1.73	1.3	6.32	2.2	0.072	1.2	6.32	2.2	0.0729	2.9	948	20
OBM-1-12.1	66.0	404	1638	3.0	1.44	1.4	5.85	2.8	0.079	1.2	5.85	2.8	0.0730	4.0	1017	27
OBM-1-13.1	22.9	172	8398	3.2	2.03	2.3	5.76	2.6	0.087	0.2	5.77	2.6	0.0729	9.7	1031	25
OBM-1-14.1	108.1	632	5048	3.7	1.47	1.2	6.12	2.0	0.072	1.0	6.12	2.0	0.0729	2.1	976	19
OBM-1-15.1	74.7	558	1840	3.0	1.86	1.2	5.80	1.8	0.078	1.1	5.80	1.8	0.0731	3.6	1026	17
OBM-1-16.1	97.4	678	2683	3.0	1.75	1.0	5.57	1.8	0.078	0.9	5.57	1.8	0.0730	2.0	1065	18

[a]Isotope ratios corrected for initial Pb using 1Ga Stacey-Kramers (S-K) model Pb composition ($^{206}Pb/^{204}Pb$ =17.068, $^{207}Pb/^{204}Pb$ = 15.510) and the measured abundance of ^{204}Pb.

[b]Age (Ma) calculated from the $^{206}Pb^*/^{238}U$ ratio corrected for the initial Pb using S-K model.

Fig. 1. Simplified geologic map of the southern Grenville Province. Modified from CHIARENZELLI et al. (2018), MCLELLAND AND SELLECK, (2011), and LUPULESCU et al. 2017.

Fig. 2. Backscattered electron (BSE) images of selected apatite grains from McClure Mountain (A and B), Cheever mine (C and D), and Old Bed mine (E and F). Mnz – monazite, Mt – magnetite.

Fig. 3. Backscattered electron (BSE) images of magnetite ore from the Old Bed mine. Ap – apatite, Mnz – monazite, Mt – magnetite, Qtz – quartz.

Fig. 4. Electron probe microanalysis elemental maps for Th, Si, Sr and Y from Cheever mine (A and B) and Old Bed mine (C and D) apatite.

Fig. 5. U-Pb isotope-dilution thermal ionization mass spectrometry results for Cheever mine apatite. A-- ^{238}U-^{206}Pb (A), B--^{235}U-^{207}Pb, and C--the Total-Pb/U isochron diagrams.

Fig. 6. U-Pb isotope-dilution thermal ionization mass spectrometry results for Old Bed mine apatite. A--^{238}U-^{206}Pb, B-- ^{235}U-^{207}Pb, and C-- Total-Pb/U (C) diagrams.

Fig. 7. U-Pb isotope-dilution thermal ionization mass spectrometry results for McClure Mountain apatite. A--^{238}U-^{206}Pb, B--^{235}U-^{207}Pb, and C-- Total-Pb/U (C) diagrams.

Fig. 8. Old Bed mine (OBM) zircon. A – transmitted light, B – cathodoluminescence image, C and D – Concordia diagrams for cores and rims, respectively (sensitive high-resolution ion microprobe SHRIMP II data, Table 3). The diameter of the spot is 25 μm.

Fig. 9. Tera-Wasserburg isochron for sensitive high-resolution ion microprobe-reverse geometry SHRIMP-RG U-Pb data for Old Bed mine (OBM) apatite. A – Stacey-Kramers initial Pb corrected (1 Ga) and B – initial-Pb-uncorrected.

Fig. 10. Laser ablation inductively-coupled plasma mass spectrometry Tera-Wasserburg isochron for low-U Cheever mine apatite.

Fig. 11. Tera-Wasserburg isochrons for Old Bed mine (OBM) apatite normalised to McClure Mountain apatite as a matrix matched standard. A – anchored and B – unconstrained.

Fig. 12. Tera-Wasserburg isochron for laser ablation inductively-coupled plasma mass spectrometry U-Pb data for the Cheever mine apatite (Table EA 5).

Fig. 13. Concordia diagrams showing effects of different initial Pb isotope composition corrections on the U-Pb data. A and B – McClure Mountain with correction from the total Pb/U isochron and Stacey-Kramers model, respectively, C – Cheever mine, D – S-K model corrected data for Cheever mine apatite, E – Old Bed mine, F – S-K model corrected data for Old Bed mine apatite.

Fig. 14. Two Tera-Wasserburg isochrons for the Old Bed mine apatite raw data anchored to the Stacey-Kramers model (S-K, green dashed line) and $^{207}Pb/^{206}Pb$ = 0.186 (blue dashed

line) Y-axis intercepts. A correction factor calculated as $F = R_t)/r_{b2}$ results in an overestimated correction for the matrix effect. A more accurate correction should use the $F = R_t/R_{b2}$. The R_{b2} value can be calculated from the equation for the blue regression line for $y = R_t$. In case of the S-K Y-axis intercept and much steeper slope of the green isochron the age difference is essentially negligible because $R_{b1} \approx r_{b1}$.

Fig. 15. The Pb-Pb plot showing a two-point paleo-isochron passing through the initial Pb compositions of Cheever mine and Old Bed mine apatite. Inset shows the Stacey-Kramers model curve of Pb evolution (second stage) and paleo-isochron (dotted line).

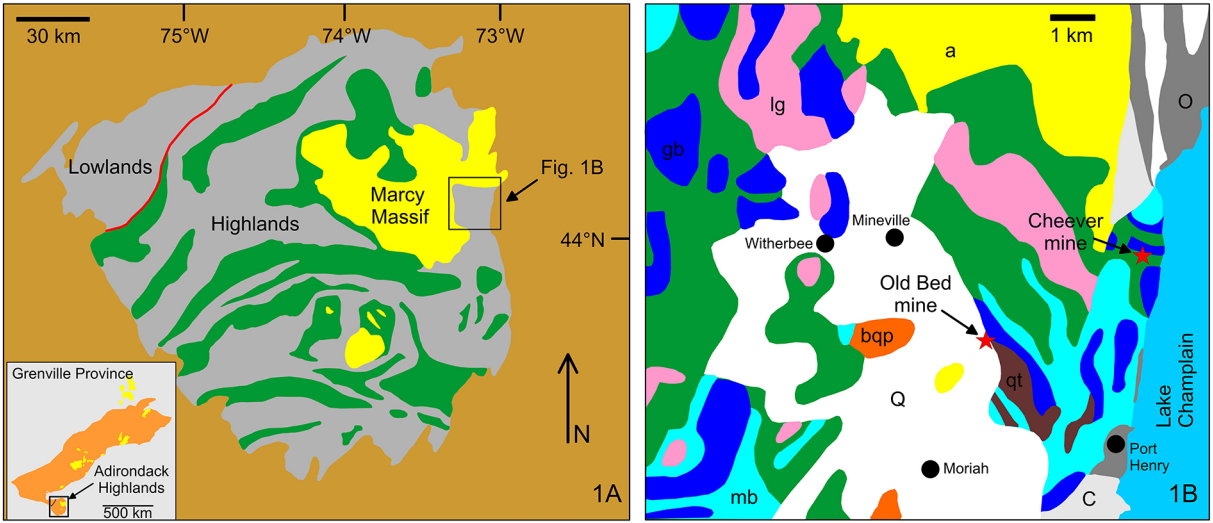
Fig. 16. Summary of geochronological data from CHIARENZELLI et al. (2018)[1], REGAN et al. (2019)[2], and this study.

Journal Pre-proof

Declaration of interests

☒ The authors declare that they have no known competing financial interests or personal relationships that could have appeared to influence the work reported in this paper.

Journal Pre-proof



Legend

Paleozoic rocks	Q	Quaternary deposits	mb	Marble
Mixed metasedimentary and metaigneous rocks	O	Ordovician rocks	bqp	Pelitic gneiss
Mangerite - charnockite	C	Cambrian rocks	qt	Quartzite
a Anorthosite	lg	Leucogranite	★	Mine
Carthage/Colton Mylonite zone	gb	Gabbro	●	Town

Figure 1

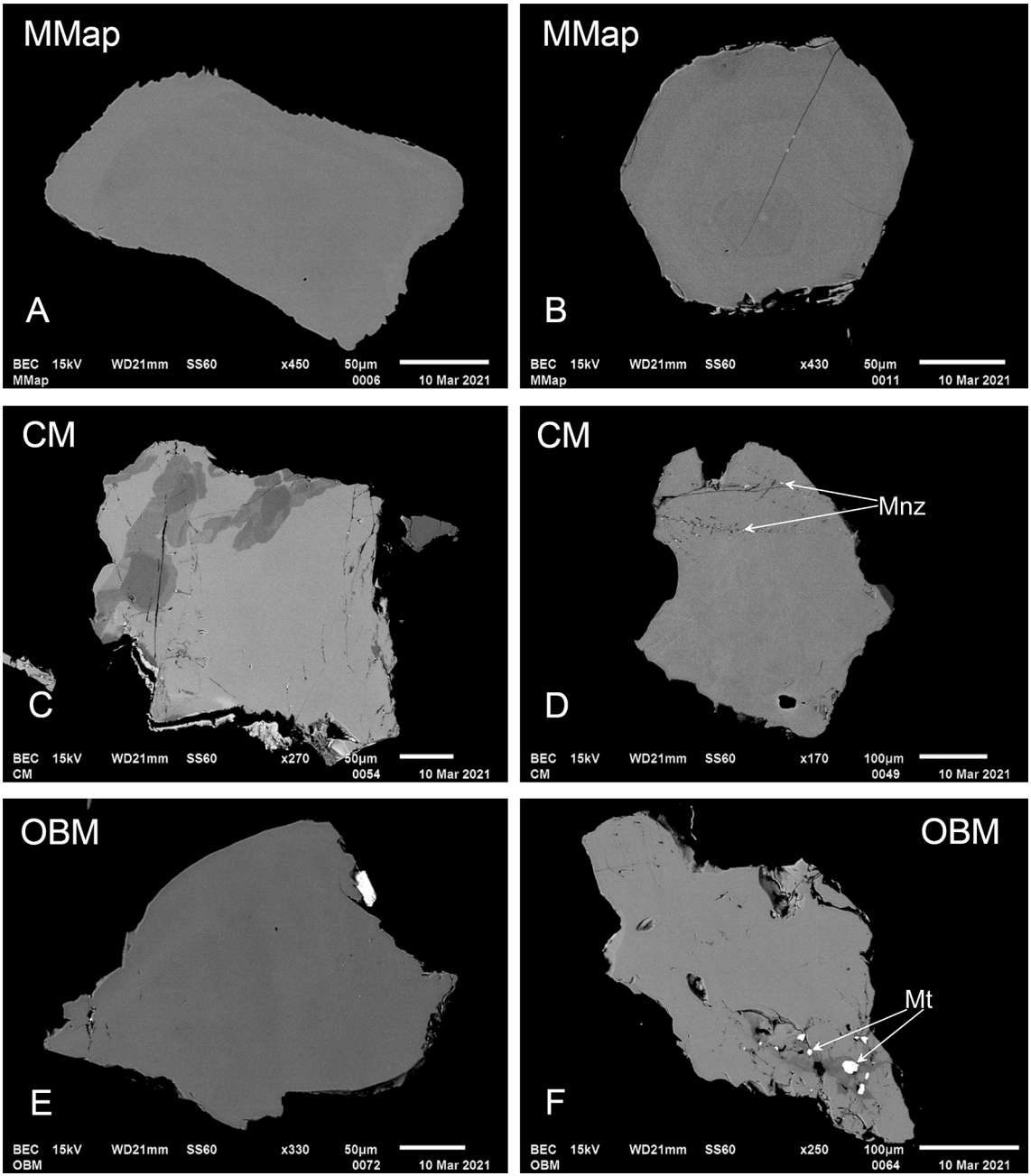

MMap
A
BEC 15kV WD21mm SS60 x450 50µm
MMap 0006 10 Mar 2021
MMap
B
BEC 15kV WD21mm SS60 x430 50µm
MMap 0011 10 Mar 2021
CM
C
BEC 15kV WD21mm SS60 x270 50µm
CM 0054 10 Mar 2021
CM
Mnz
D
BEC 15kV WD21mm SS60 x170 100µm
CM 0049 10 Mar 2021
OBM
E
BEC 15kV WD21mm SS60 x330 50µm
OBM 0072 10 Mar 2021
OBM
Mt
F
BEC 15kV WD21mm SS60 x250 100µm
OBM 0064 10 Mar 2021

Figure 2

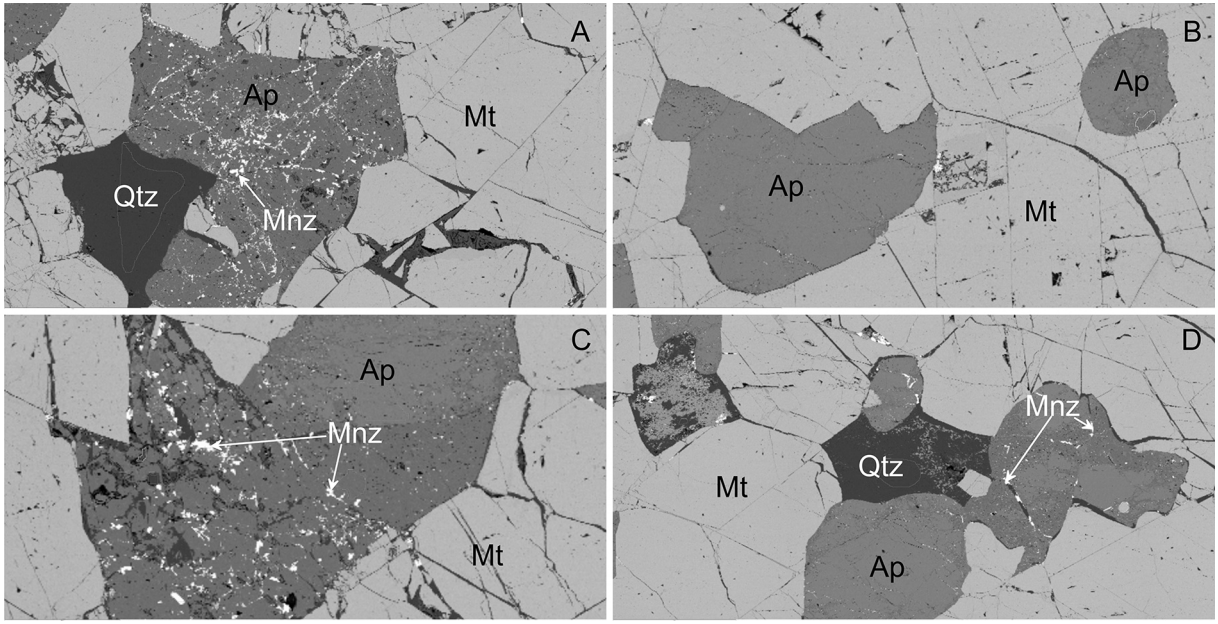


Figure 3

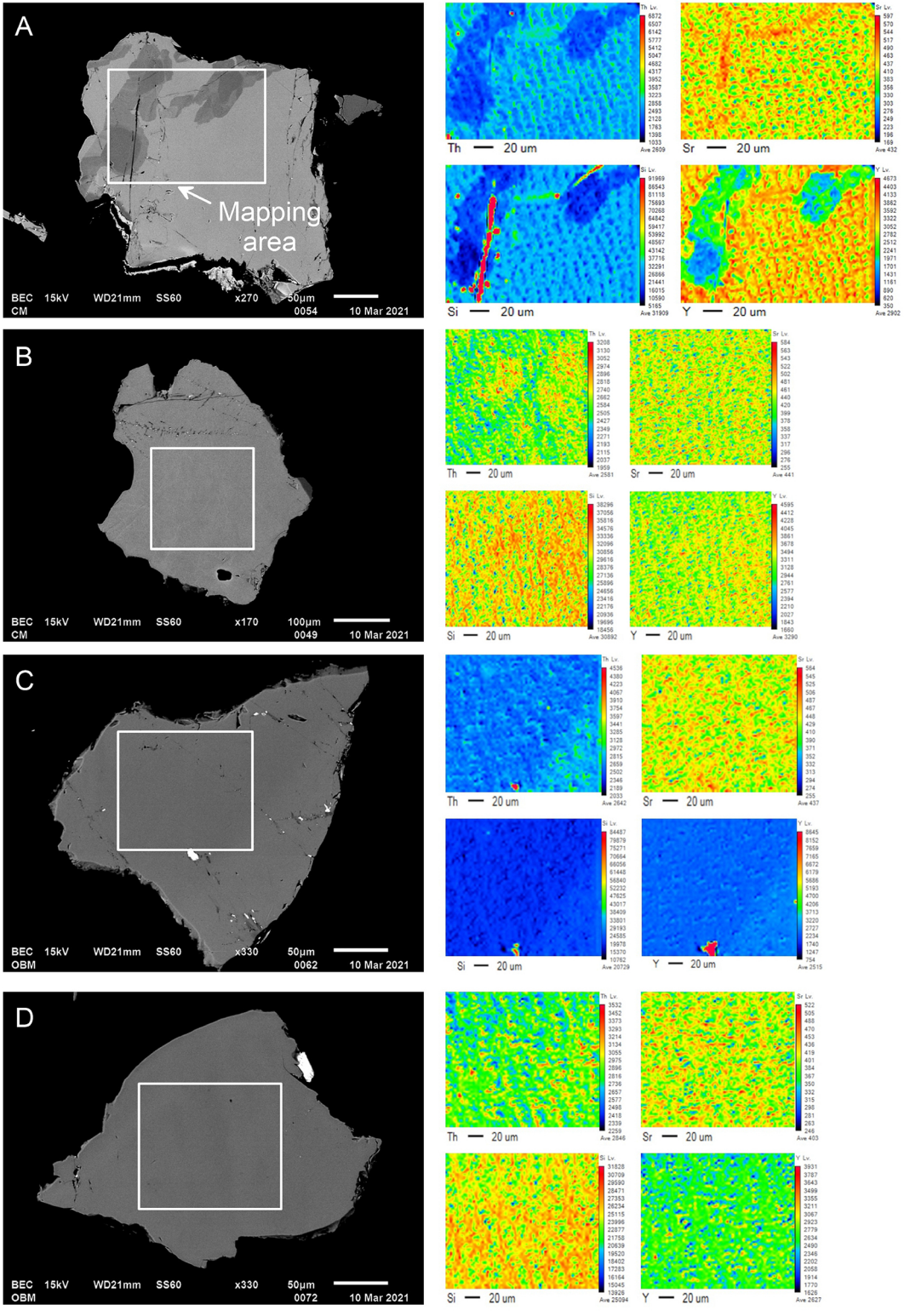

A
Mapping area
BEC 15kV WD21mm SS60 x270 50µm
CM 0054 10 Mar 2021
Th 20 um
Sr 20 um
Si 20 um
Y 20 um
B
BEC 15kV WD21mm SS60 x170 100µm
CM 0049 10 Mar 2021
Th 20 um
Sr 20 um
Si 20 um
Y 20 um
C
BEC 15kV WD21mm SS60 x330 50µm
OBM 0062 10 Mar 2021
Th 20 um
Sr 20 um
Si 20 um
Y 20 um
D
BEC 15kV WD21mm SS60 x330 50µm
OBM 0072 10 Mar 2021
Th 20 um
Sr 20 um
Si 20 um
Y 20 um

Figure 4

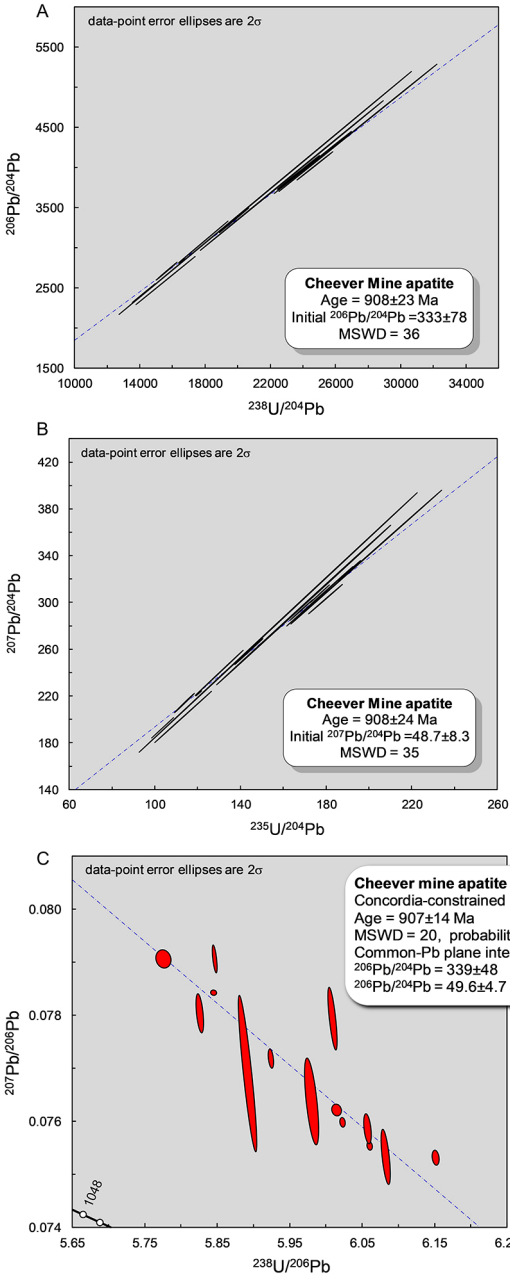
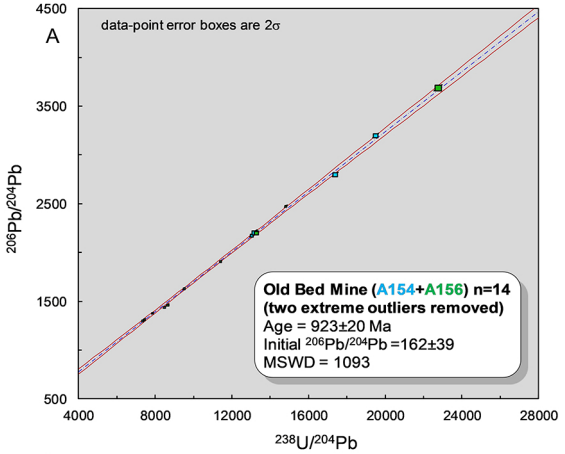
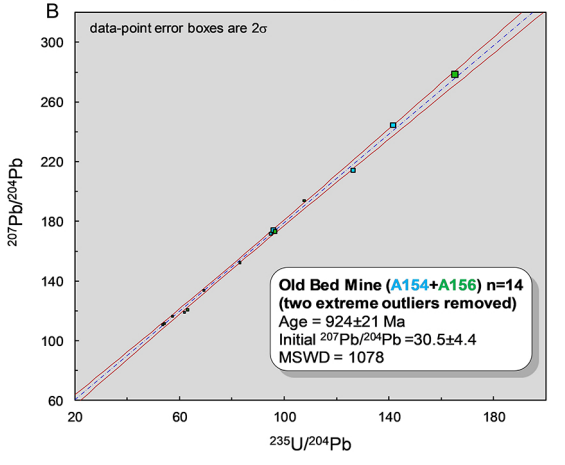

A
data-point error ellipses are 2σ
Cheever Mine apatite
Age = 908±23 Ma
Initial 206Pb/204Pb =333±78
MSWD = 36
206Pb/204Pb
238U/204Pb
B
data-point error ellipses are 2σ
Cheever Mine apatite
Age = 908±24 Ma
Initial 207Pb/204Pb =48.7±8.3
MSWD = 35
207Pb/204Pb
235U/204Pb
C
data-point error ellipses are 2σ
Cheever mine apatite
Concordia-constrained linear 3-D isochron
Age = 907±14 Ma
MSWD = 20, probability =0.000
Common-Pb plane intercepts at
206Pb/204Pb = 339±48
206Pb/204Pb = 49.6±4.7
1048
207Pb/206Pb
238U/206Pb

Figure 5


A
data-point error boxes are 2σ
Old Bed Mine (A154+A156) n=14
(two extreme outliers removed)
Age = 923±20 Ma
Initial 206Pb/204Pb =162±39
MSWD = 1093
206Pb/204Pb
238U/204Pb
4500
3500
2500
1500
500
4000
8000
12000
16000
20000
24000
28000


B
data-point error boxes are 2σ
Old Bed Mine (A154+A156) n=14
(two extreme outliers removed)
Age = 924±21 Ma
Initial 207Pb/204Pb =30.5±4.4
MSWD = 1078
207Pb/204Pb
235U/204Pb
300
260
220
180
140
100
60
20
60
100
140
180

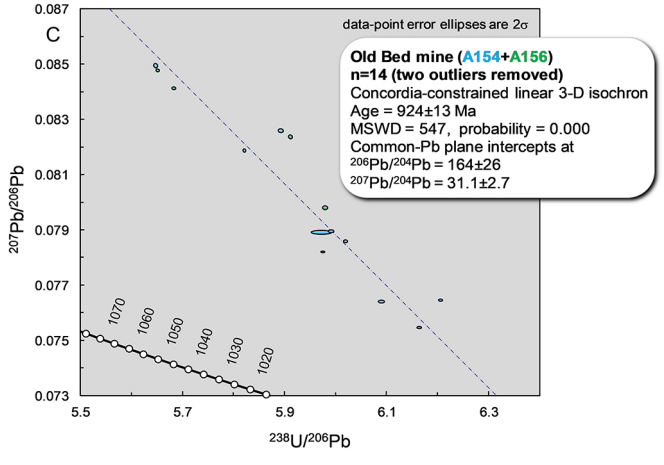

C
data-point error ellipses are 2σ
Old Bed mine (A154+A156)
n=14 (two outliers removed)
Concordia-constrained linear 3-D isochron
Age = 924±13 Ma
MSWD = 547, probability = 0.000
Common-Pb plane intercepts at
206Pb/204Pb = 164±26
207Pb/204Pb = 31.1±2.7
207Pb/206Pb
238U/206Pb
0.087
0.085
0.083
0.081
0.079
0.077
0.075
0.073
5.5
5.7
5.9
6.1
6.3
1070
1060
1050
1040
1030
1020

Figure 6

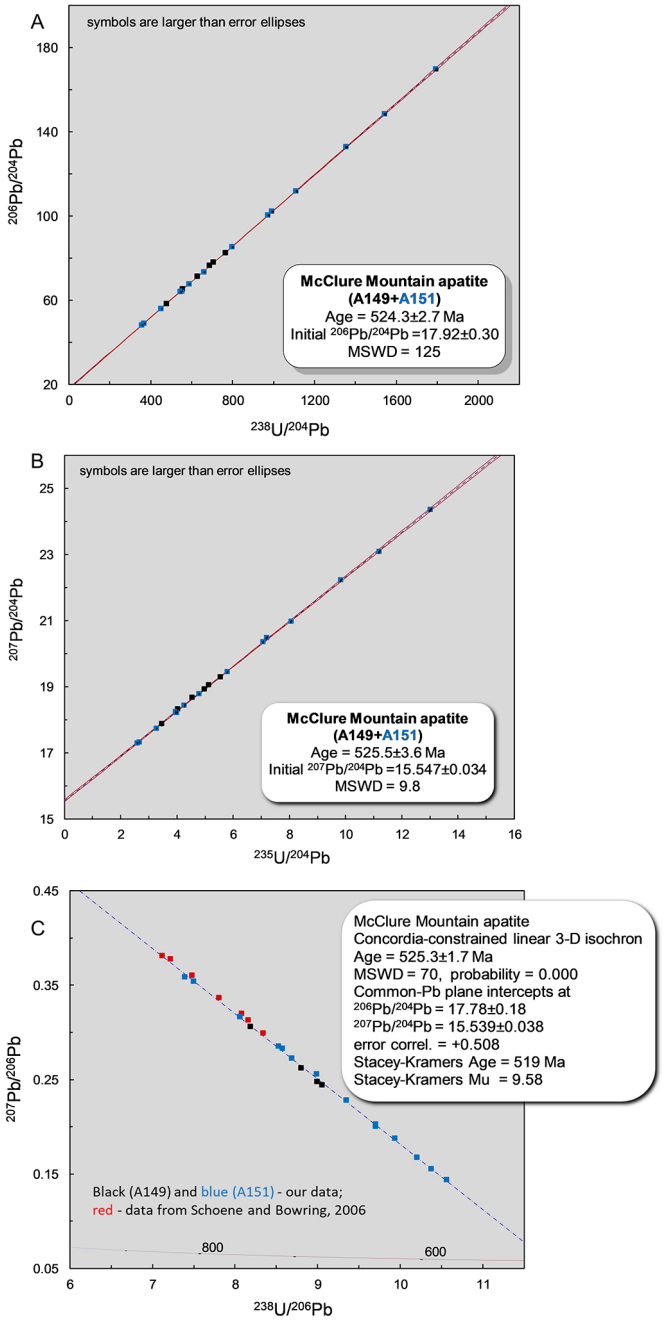

A
symbols are larger than error ellipses
$^{206}Pb/^{204}Pb$
$^{238}U/^{204}Pb$
McClure Mountain apatite
(A149+A151)
Age = 524.3±2.7 Ma
Initial $^{206}Pb/^{204}Pb$ =17.92±0.30
MSWD = 125
B
symbols are larger than error ellipses
$^{207}Pb/^{204}Pb$
$^{235}U/^{204}Pb$
McClure Mountain apatite
(A149+A151)
Age = 525.5±3.6 Ma
Initial $^{207}Pb/^{204}Pb$ =15.547±0.034
MSWD = 9.8
C
$^{207}Pb/^{206}Pb$
$^{238}U/^{206}Pb$
McClure Mountain apatite
Concordia-constrained linear 3-D isochron
Age = 525.3±1.7 Ma
MSWD = 70, probability = 0.000
Common-Pb plane intercepts at
$^{206}Pb/^{204}Pb$ = 17.78±0.18
$^{207}Pb/^{204}Pb$ = 15.539±0.038
error correl. = +0.508
Stacey-Kramers Age = 519 Ma
Stacey-Kramers Mu = 9.58
Black (A149) and blue (A151) - our data;
red - data from Schoene and Bowring, 2006
800
600

Figure 7

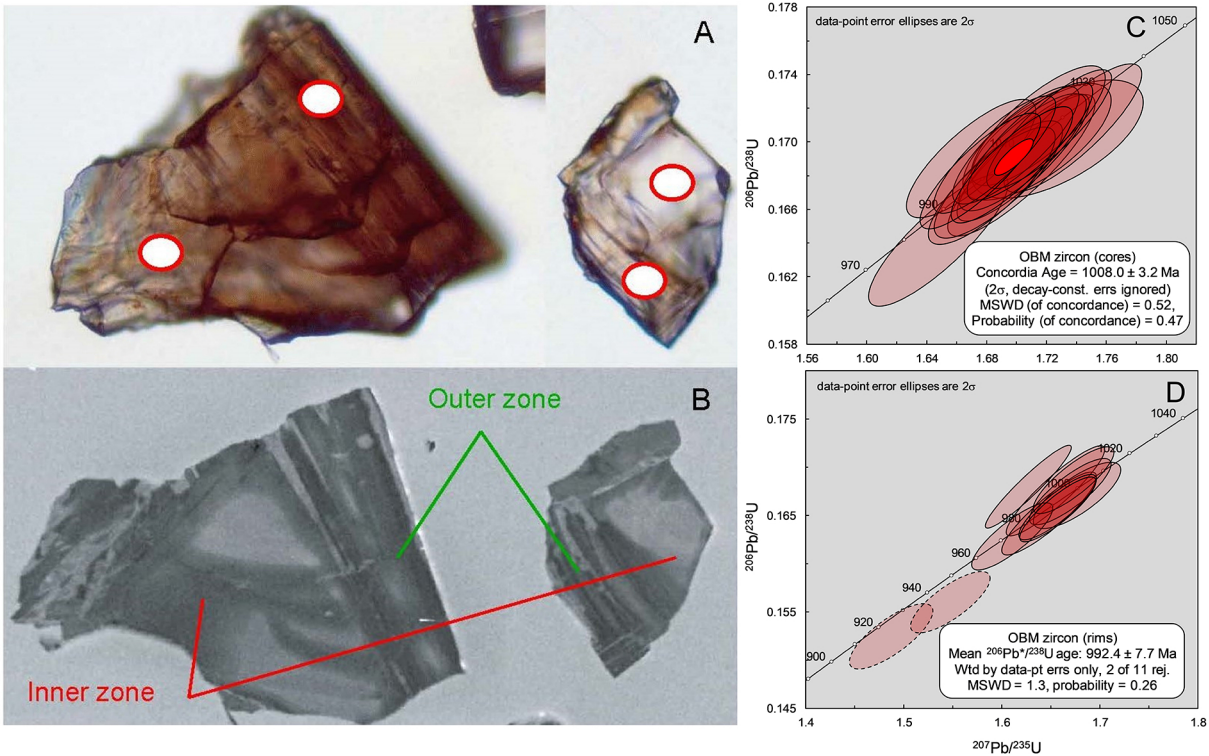

A
B
Outer zone
Inner zone
C
data-point error ellipses are 2σ
OBM zircon (cores)
Concordia Age = 1008.0 ± 3.2 Ma
(2σ, decay-const. errs ignored)
MSWD (of concordance) = 0.52,
Probability (of concordance) = 0.47
D
data-point error ellipses are 2σ
OBM zircon (rims)
Mean 206Pb*/238U age: 992.4 ± 7.7 Ma
Wtd by data-pt errs only, 2 of 11 rej.
MSWD = 1.3, probability = 0.26
206Pb/238U
207Pb/235U

Figure 8

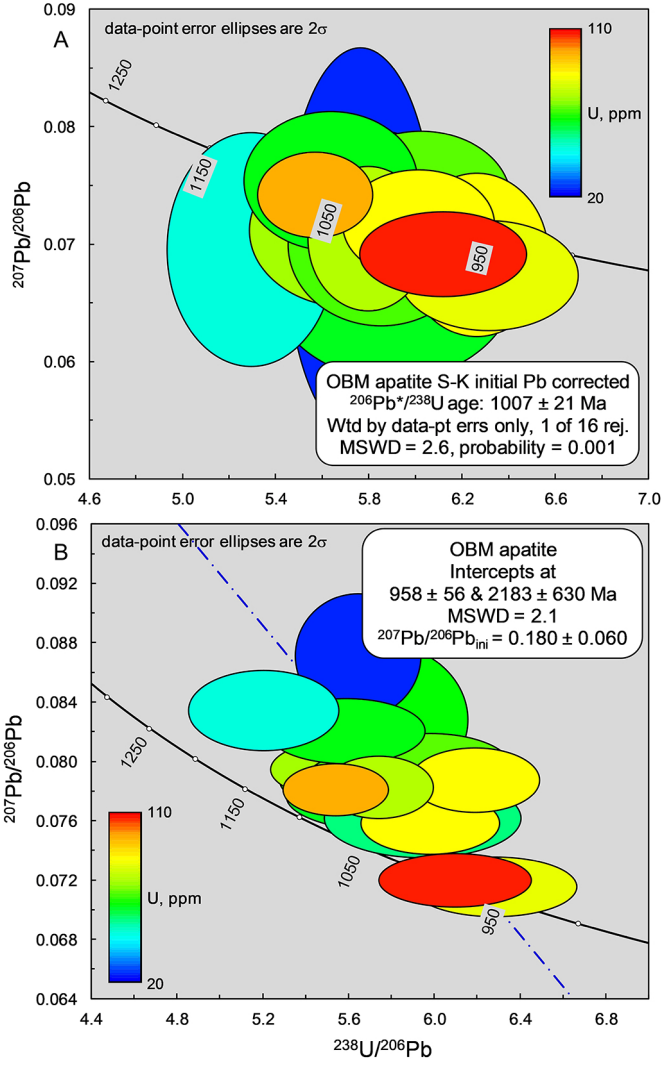

A
data-point error ellipses are 2σ
110
U, ppm
20
1250
1150
1050
950
OBM apatite S-K initial Pb corrected
206Pb*/238U age: 1007 ± 21 Ma
Wtd by data-pt errs only, 1 of 16 rej.
MSWD = 2.6, probability = 0.001
207Pb/206Pb
0.09
0.08
0.07
0.06
0.05
4.6
5.0
5.4
5.8
6.2
6.6
7.0
B
data-point error ellipses are 2σ
OBM apatite
Intercepts at
958 ± 56 & 2183 ± 630 Ma
MSWD = 2.1
207Pb/206Pbini = 0.180 ± 0.060
110
U, ppm
20
1250
1150
1050
950
207Pb/206Pb
0.096
0.092
0.088
0.084
0.080
0.076
0.072
0.068
0.064
4.4
4.8
5.2
5.6
6.0
6.4
6.8
238U/206Pb

Figure 9

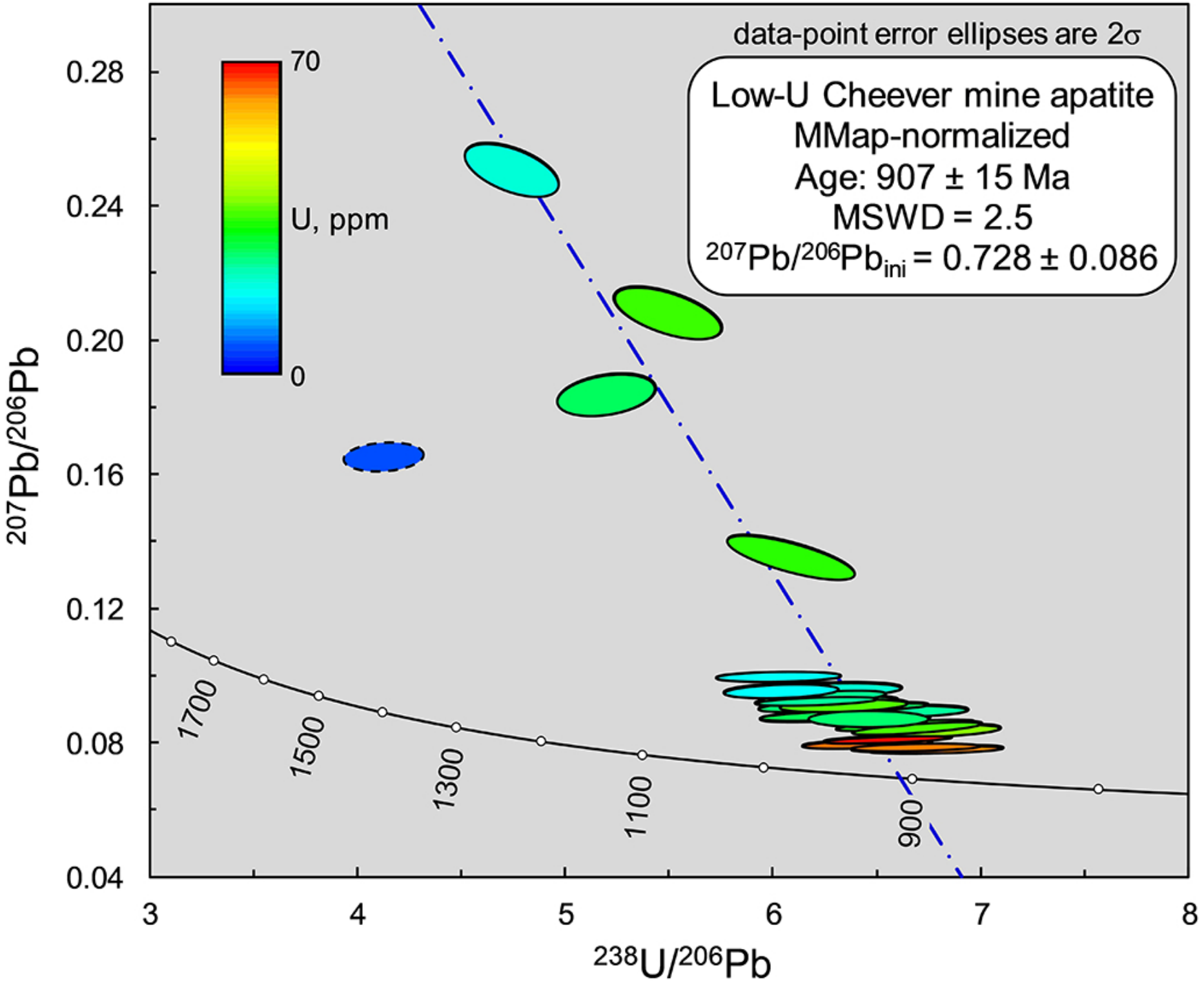

data-point error ellipses are 2σ
Low-U Cheever mine apatite
MMap-normalized
Age: 907 ± 15 Ma
MSWD = 2.5
207Pb/206Pbini = 0.728 ± 0.086
70
U, ppm
0
0.28
0.24
0.20
0.16
0.12
0.08
0.04
207Pb/206Pb
3
4
5
6
7
8
238U/206Pb
1700
1500
1300
1100
900

Figure 10

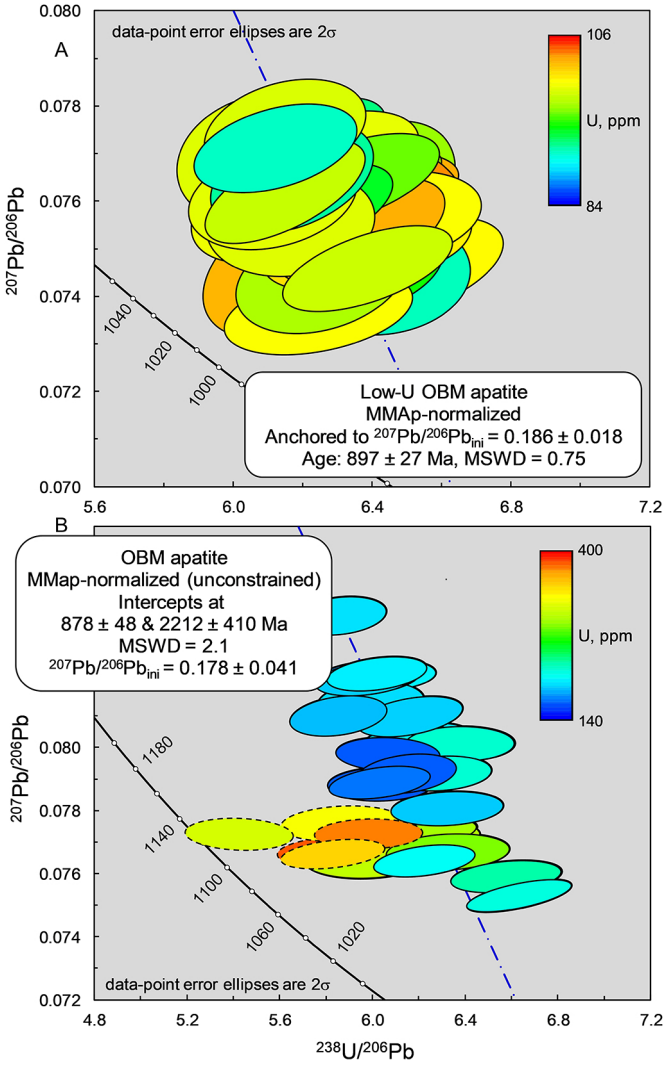

A
data-point error ellipses are 2σ
106
U, ppm
84
0.080
0.078
0.076
0.074
0.072
0.070
$^{207}Pb/^{206}Pb$
1040
1020
1000
Low-U OBM apatite
MMAp-normalized
Anchored to $^{207}Pb/^{206}Pb_{ini}$ = 0.186 ± 0.018
Age: 897 ± 27 Ma, MSWD = 0.75
5.6
6.0
6.4
6.8
7.2
B
OBM apatite
MMap-normalized (unconstrained)
Intercepts at
878 ± 48 & 2212 ± 410 Ma
MSWD = 2.1
$^{207}Pb/^{206}Pb_{ini}$ = 0.178 ± 0.041
400
U, ppm
140
1180
1140
1100
1060
1020
data-point error ellipses are 2σ
4.8
5.2
5.6
6.0
6.4
6.8
7.2
$^{238}U/^{206}Pb$

Figure 11

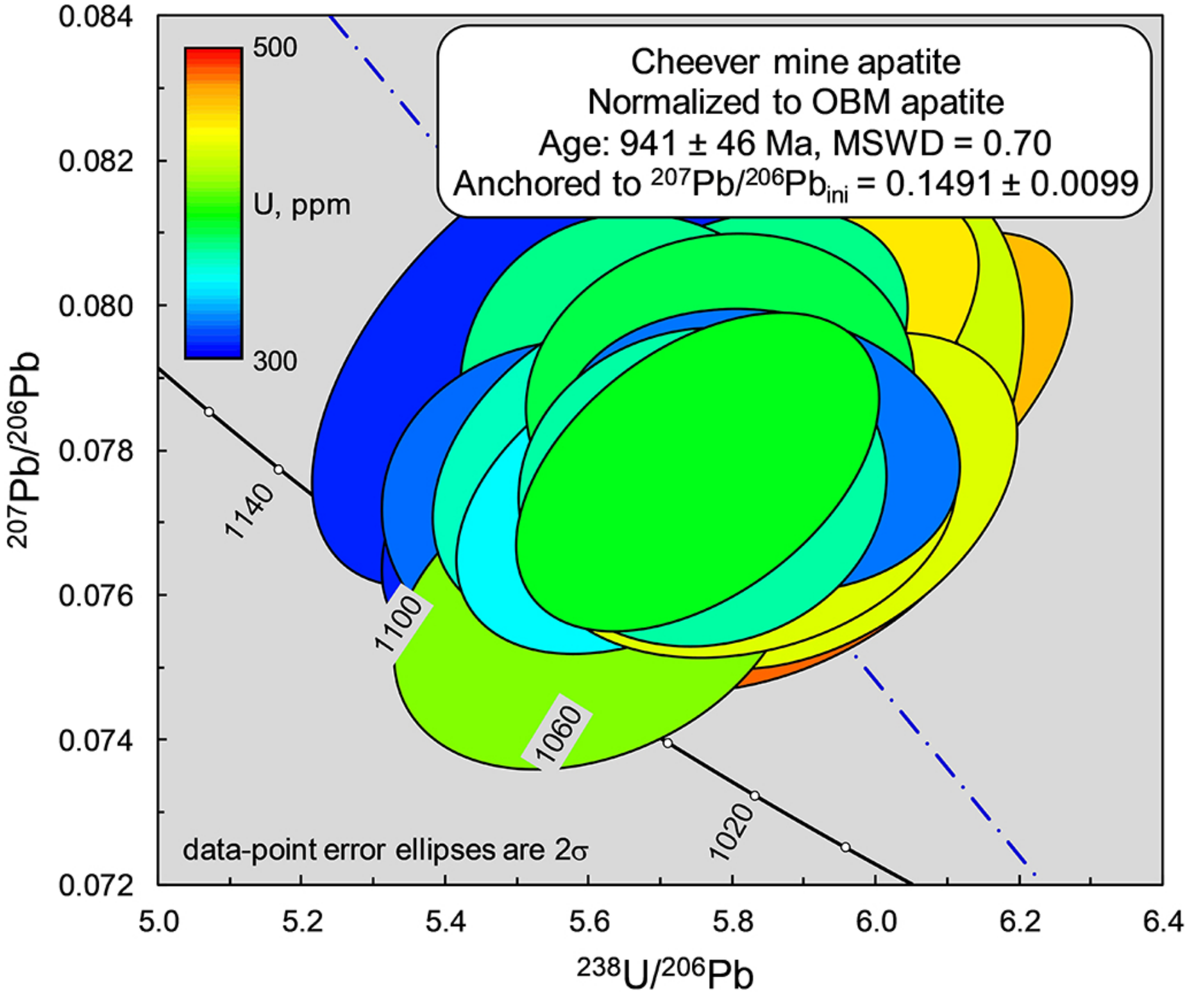

Cheever mine apatite
Normalized to OBM apatite
Age: 941 ± 46 Ma, MSWD = 0.70
Anchored to 207Pb/206Pbini = 0.1491 ± 0.0099
500
U, ppm
300
1140
1100
1060
1020
data-point error ellipses are 2σ
0.084
0.082
0.080
0.078
0.076
0.074
0.072
5.0
5.2
5.4
5.6
5.8
6.0
6.2
6.4
207Pb/206Pb
238U/206Pb

Figure 12

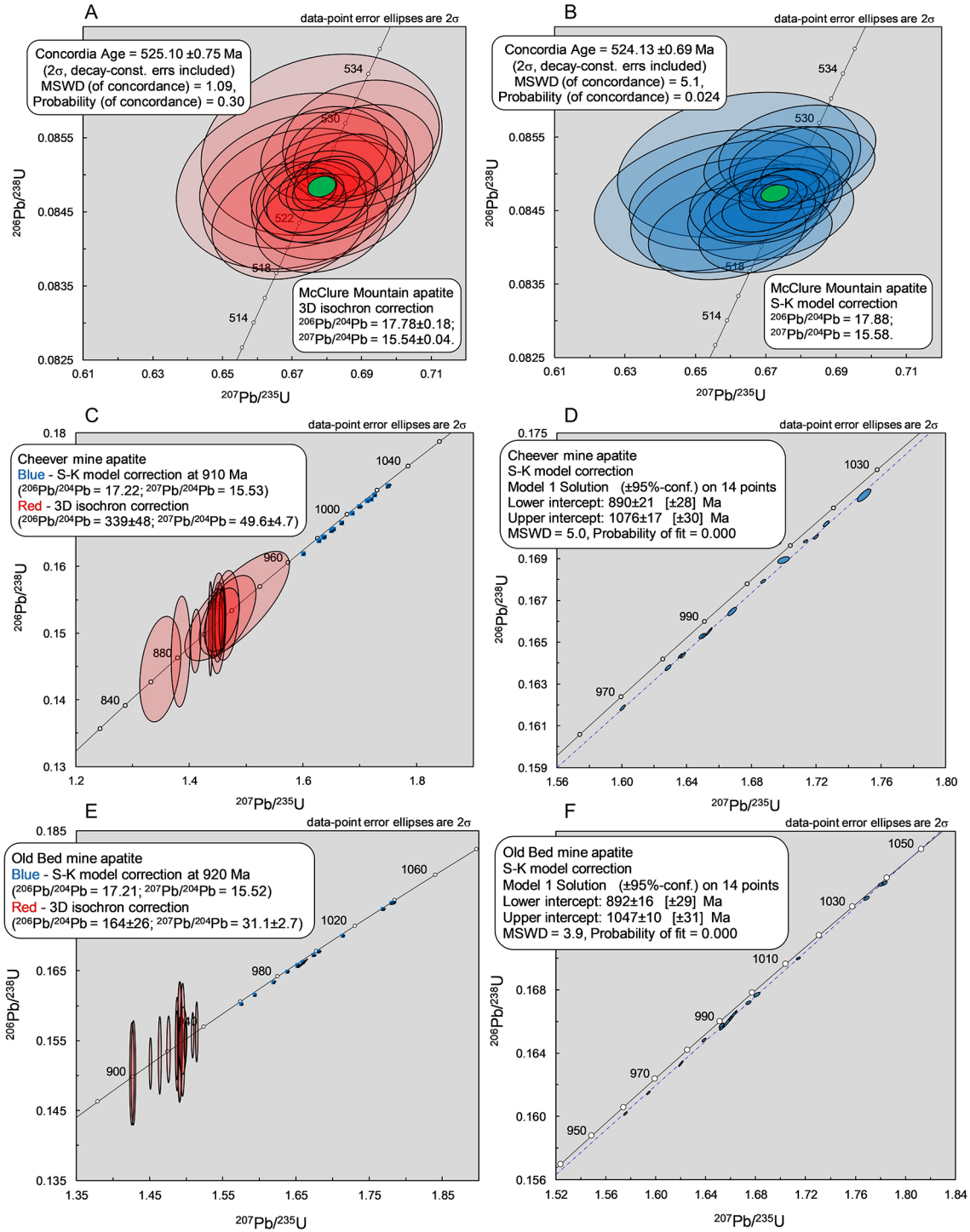
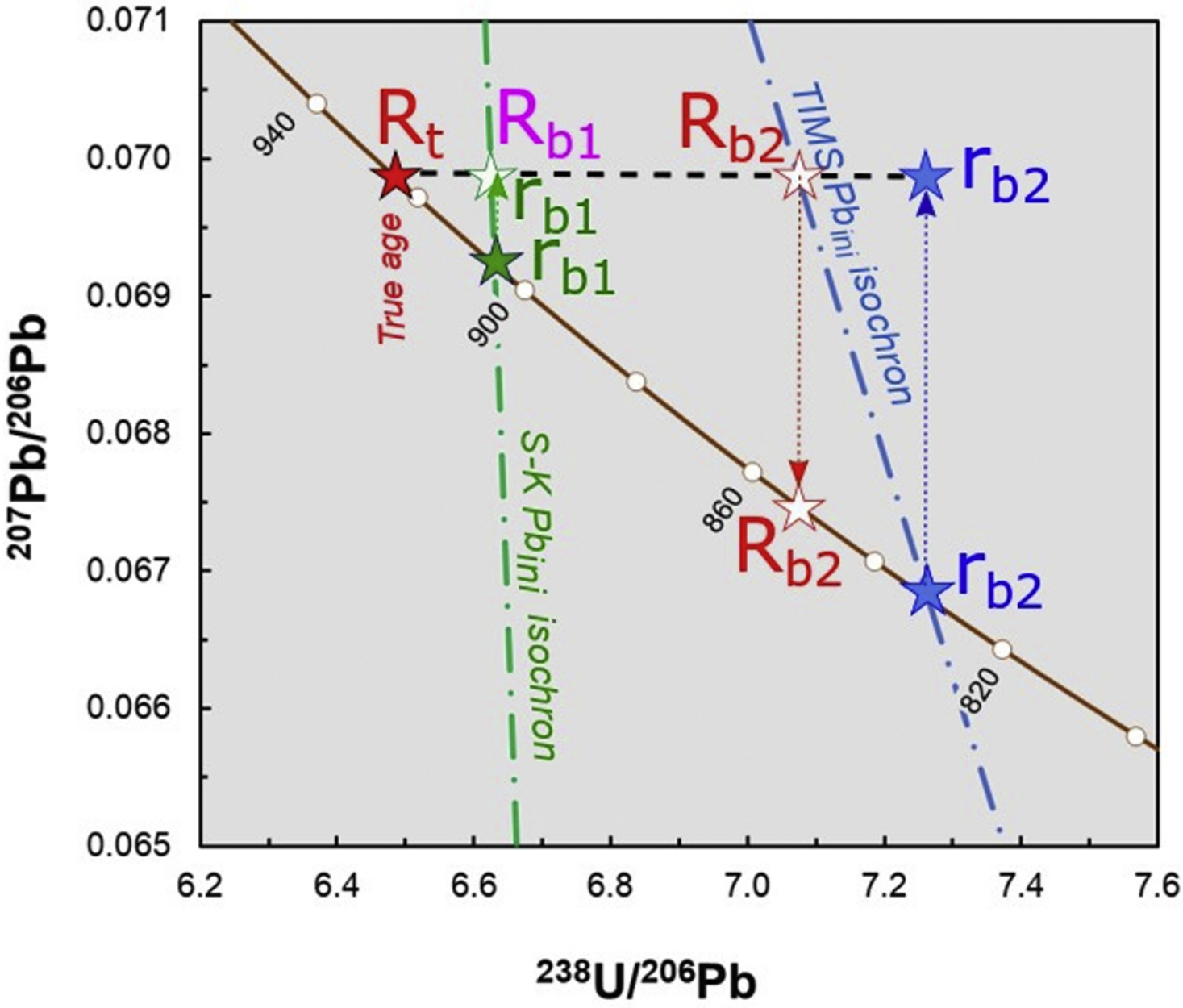

A
data-point error ellipses are 2σ
Concordia Age = 525.10 ±0.75 Ma
(2σ, decay-const. errs included)
MSWD (of concordance) = 1.09,
Probability (of concordance) = 0.30
McClure Mountain apatite
3D isochron correction
206Pb/204Pb = 17.78±0.18;
207Pb/204Pb = 15.54±0.04.
206Pb/238U
207Pb/235U
B
data-point error ellipses are 2σ
Concordia Age = 524.13 ±0.69 Ma
(2σ, decay-const. errs included)
MSWD (of concordance) = 5.1,
Probability (of concordance) = 0.024
McClure Mountain apatite
S-K model correction
206Pb/204Pb = 17.88;
207Pb/204Pb = 15.58.
C
data-point error ellipses are 2σ
Cheever mine apatite
Blue - S-K model correction at 910 Ma
(206Pb/204Pb = 17.22; 207Pb/204Pb = 15.53)
Red - 3D isochron correction
(206Pb/204Pb = 339±48; 207Pb/204Pb = 49.6±4.7)
D
data-point error ellipses are 2σ
Cheever mine apatite
S-K model correction
Model 1 Solution (±95%-conf.) on 14 points
Lower intercept: 890±21 [±28] Ma
Upper intercept: 1076±17 [±30] Ma
MSWD = 5.0, Probability of fit = 0.000
E
data-point error ellipses are 2σ
Old Bed mine apatite
Blue - S-K model correction at 920 Ma
(206Pb/204Pb = 17.21; 207Pb/204Pb = 15.52)
Red - 3D isochron correction
(206Pb/204Pb = 164±26; 207Pb/204Pb = 31.1±2.7)
F
data-point error ellipses are 2σ
Old Bed mine apatite
S-K model correction
Model 1 Solution (±95%-conf.) on 14 points
Lower intercept: 892±16 [±29] Ma
Upper intercept: 1047±10 [±31] Ma
MSWD = 3.9, Probability of fit = 0.000

Figure 13



OBM Apatite
S-K common Pb corrected
Raw "age" : 906 ± 10 Ma, MSWD = 1.08
TIMS radiogenic Pb_{ini} corrected
Raw "age" : 831 ± 37 Ma, MSWD = 0.65

Figure 14

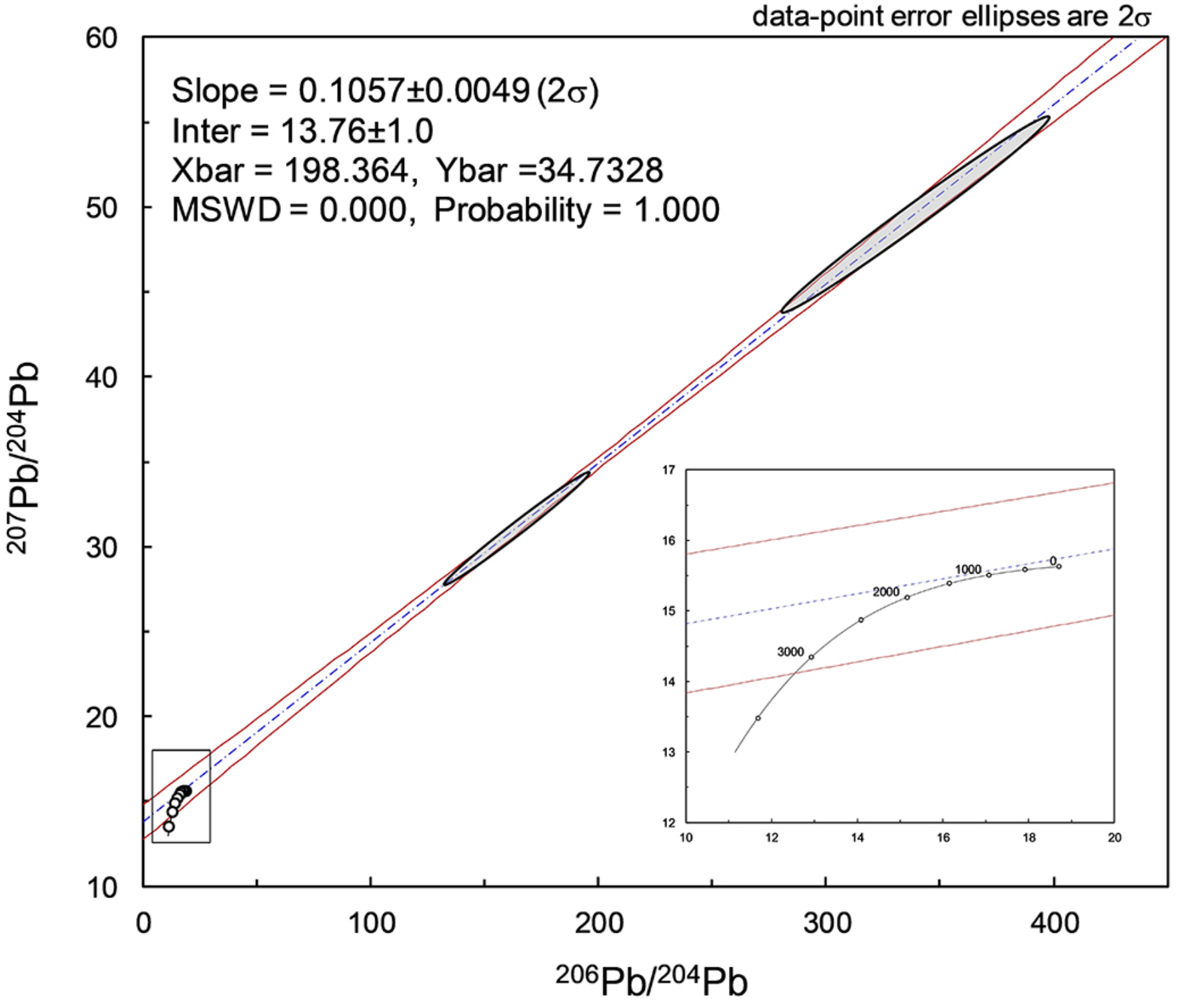

data-point error ellipses are 2σ
Slope = 0.1057±0.0049 (2σ)
Inter = 13.76±1.0
Xbar = 198.364, Ybar =34.7328
MSWD = 0.000, Probability = 1.000
207Pb/204Pb
206Pb/204Pb
60
50
40
30
20
10
0
100
200
300
400
17
16
15
14
13
12
10
12
14
16
18
20
0
1000
2000
3000

Figure 15

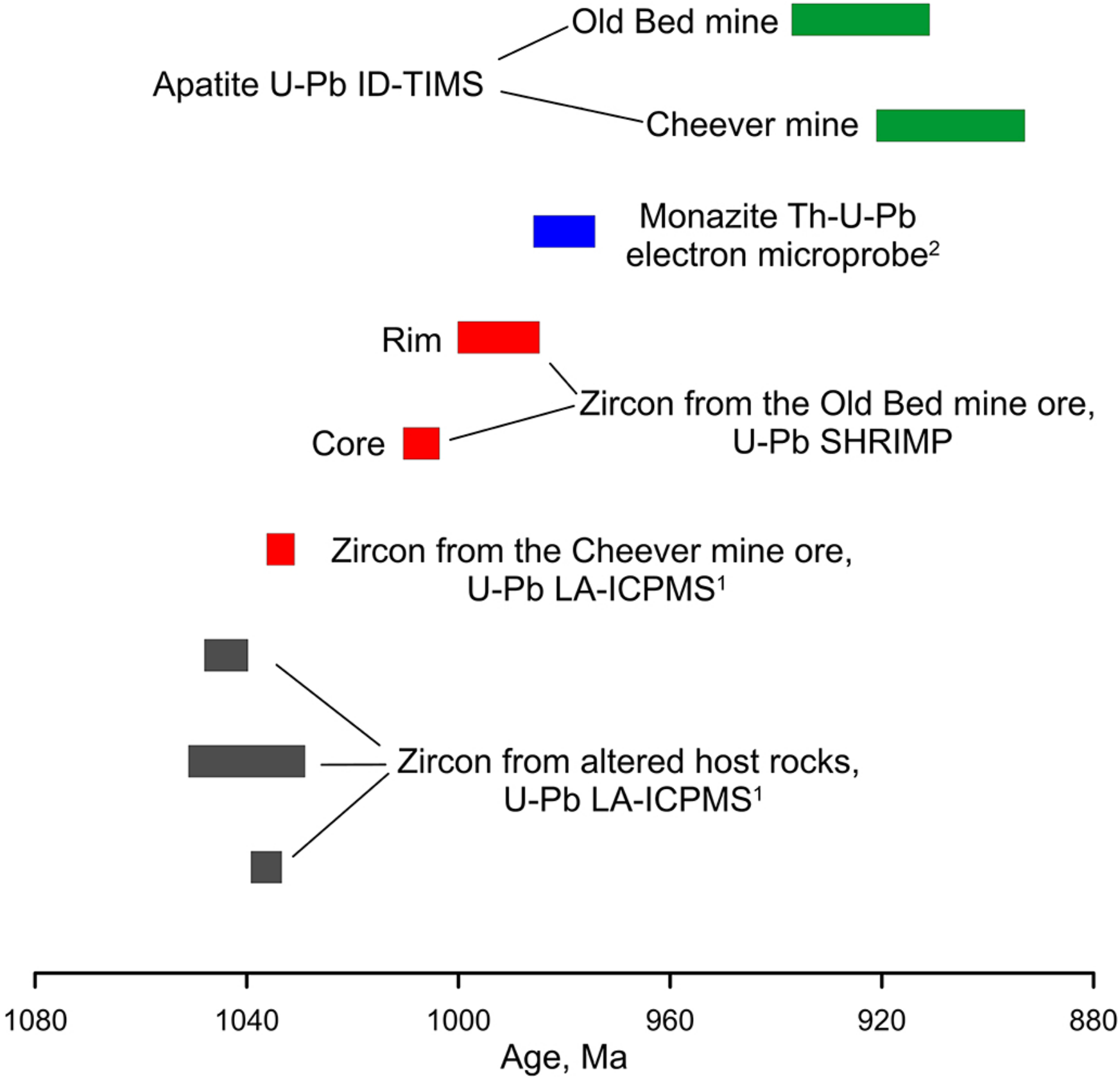

Old Bed mine
Apatite U-Pb ID-TIMS
Cheever mine
Monazite Th-U-Pb
electron microprobe[2]
Rim
Zircon from the Old Bed mine ore,
U-Pb SHRIMP
Core
Zircon from the Cheever mine ore,
U-Pb LA-ICPMS[1]
Zircon from altered host rocks,
U-Pb LA-ICPMS[1]
1080
1040
1000
960
920
880
Age, Ma

Figure 16